ALMA MATER STUDIORUM

BOLOGNA UNIVERSITY

FACULTY OF ENGINEERING

Department of Electronics, Computer Science and Systems
- DEIS

Research Doctorate in Electronics, Computer
Science and Telecommunications
XX Cycle; ING-INF/01-Electronics

CONTROL OF THE POSITION OF PARTICLES IN OPEN MICROFLUIDIC SYSTEMS

Presented by
Daniele Gazzola

Advisor
Prof. **Roberto Guerrieri**

Coordinator
Prof. **Paolo Bassi**

Final Exam 2008

---

to time and space

time never failed me
maintain, fix, and let go

my way is to whom whatever, wherever stayed, just more than one
needs: a healthy too much.
to growing kids, synergy and stability and going around and around it

space is my freedom
wherever a home

my day is to my secret share
to my spread self
to the awway sound
to the eccentric animals I gave myself, and they did
to the boundaries, and the lack of them
to the warm harassment, I would be less, otherwise

in time and space is where you thought myself

and to whom I can't decide if space or time, because is the sea or the
sky on my skin

Keywords

Evaporation

Transpiration

Convective flows

Marangoni Effect

Microfluidics

Lab on a Chip

Index of equations

$$\frac{\Delta E_R}{E_{R,avg}} = 2\frac{(100\% - 24\%) - (100\% - 37\%)}{(100\% - 24\%) + (100\% - 37\%)} = 19\% \quad (2.16) \quad 34$$

$$C_{cop} = \frac{2\varepsilon_0\varepsilon_r l}{\pi}\ln\left[\left(1+\frac{w}{a}\right)+\sqrt{\left(1+\frac{w}{a}\right)^2-1}\right] \quad (2.17) \quad 38$$

$$C_{par} = \varepsilon_0\varepsilon_r\frac{lh}{2a} \quad (2.18) \quad 39$$

$$C_{diff} = \varepsilon_0\varepsilon_r k = \sqrt{\frac{2\cdot 10^{-3} z^2 e^2 \varepsilon_0\varepsilon_r C N_A}{k_B T}} \quad (2.19) \quad 41$$

$$Z_W = \frac{\sigma}{\sqrt{2\omega}}(1-i) \quad (2.20) \quad 42$$

$$v_{term} = g\frac{m_{sol} - m_{part}}{6\pi\eta_{sol} a_{part}} = g\frac{2(\rho_{sol} - \rho_{part})a_{part}^2}{9\eta_{sol}} \quad (4.1) \quad 86$$

$v_{g\,PBS}$ = 1.07 um/s (4.2) 92

$v_{g\,KCl}$ = 7.1 um/s (4.3) 92

List of figures

1 Introduction

1.1Motivation

Considerable effort has been spent in the last decade to miniaturize devices for chemical and biomedical applications. Several strategies to control the motion and the position of individual particles in a fluid have been proposed in the literature. These are mainly based on optical trapping, dielectrophoresis and/or electro-osmosis induced by electric fields or by magnetic fields able to drag magnetic beads [**1**,**2**,**3**,**4**,**5**]. However the power dissipation necessarily involved in the process can produce thermal stress on the biological material.

A particle subjected to a gravitational field in a fluid medium moves at a velocity which depends on the area and mass density of the cell and on the viscosity and density of the fluid [**6**]. The sedimentation velocity of cells of interest to bio-medical applications varies from very small values to tens of micrometers per second [**7**]. As an example, the male human erythrocyte sedimentation rate increases with age from about 0.7 μm/s (20 years) to about 2 μm/s (60 years) [**8**]. Such motion of the particle in a microfluidics Lab-on-a-Chip can affect the measurements of some cell properties. Several strategies, mainly based on optical, electric or magnetic fields patterns, have therefore been presented to control the cell position. In an open micro-well the drag force which the evaporative flow exerts on the particle in the opposite direction to the gravitational force could be used for this purpose, provided that a system which is able to detect and control the evaporative flow velocity is available.

1.2 Biochips for cancer therapeutics: CoChiSe project

Recently it has been discovered that some cells from the immune system are able to recognize cancer cells. On the basis of this knowledge the CoChiSe project was born, along with the technological ability to create a biocompatible electrical device for the selection of these cells in an array biochip.

The major problem of cancer therapeutics lays in fact in the recognition of cancerous biological material, which would allow a treatment targeted to single cells. Medical cures are nowadays invasive: chemotherapy is based on a chemical compound that stops reproduction for all the cells it gets in contact with; radiotherapy makes use of high energy radiation damaging DNA. Even if DNA reparation is more efficient in healthy cells, the treatment damages all the biomaterial in proximity of the cancerous mass.

Fig. 1 Scene from the 1966 movie by Otto Klement *Fantastic Voyage*. Scientists are travelling within the human blood to cure a patient from brain blood clot.

Fig. 2 Scene from the 1966 movie by Otto Klement *Fantastic Voyage*. The submarine is parked in the inner ear.

The project is aimed at the direct recognition of cancerous cells one by one *in vivo*. If we were one of the characters of the movie *Fantastic Voyage* by Otto Klement [**9**] we could detect single cancerous cells from a miniaturized submarine (**Fig. 1, Fig. 2**) and make them harmless. Far from reality, this dream could still come in hands for real treatments. It is possible to stimulate the biological recognition of cancerous cells by cells of the immune system. Our submarine would then be a selected natural killer cell, or a lymphocyte, and we could imagine to produce a real army of these submarines fighting the war against cancer. It has been recently discovered [**10**,**11**,**12**,**13**] that within the numerous cells responsible for the immune response, only few out of ten thousand cells are able to detect tumour cells and send the signal to induce apoptosis. The aim of the CoChiSe project is to detect and collect such cells from the patient, in order to amplify them in a biological lab. The amplified cells massively transplanted in the patient body will then efficiently and selectively fight the cancerous mass single cell by single cell.

The treatment is based on an autologous transplant, where the transplanted cells come from the patient itself.

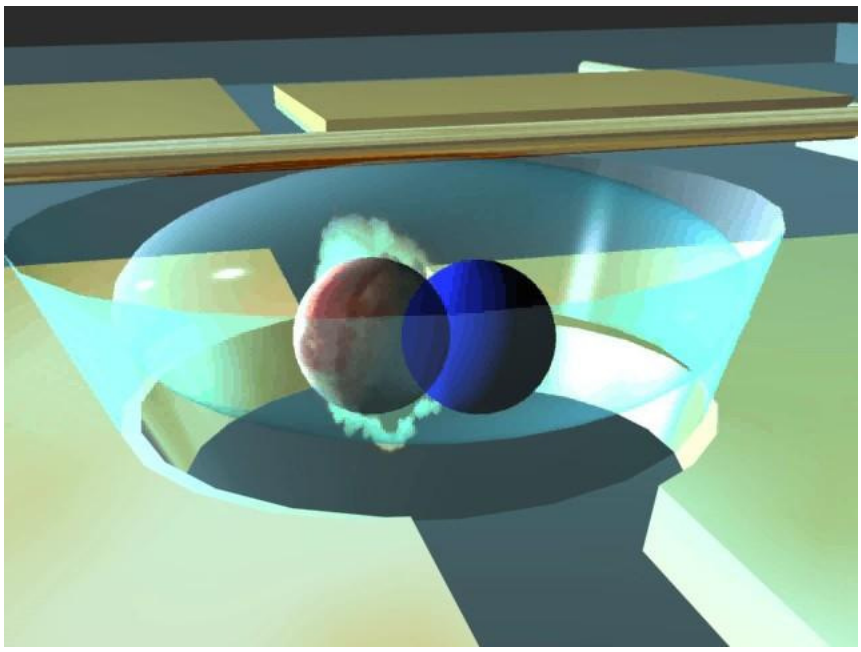

Fig. 3 The CoChiSe project is aimed to build a device able to electrically detect single cells events happening inside a microwell.

To select the correct cells it is possible to study singularly the functions of each cell while in contact with a tumour cell. In particular it is necessary to verify that the tumour cell is induced in apoptosis. In the last years a European consortium leaded by Prof. Guerrieri is working on the fabrication of an array of independent wells which will host a single tumour cell and a single cell from the immune system (**Fig. 3**). Each well will have sensors for the detection of cell apoptosis. Cell death results in the release of the cytoplasm, hence the dielectric properties of the solution in the well change. This can be quantified with an impedance measurement between two electrodes that face the well internal surface.

In order to allow the proposed technique to be used in a large array of micro-wells, circuits for impedance measurements should be integrated in a low-cost small-sized device. In particular it is planned to measure the capacitance value, which will be of the order of 10fF,

with variations of the order of the fF. Though not large, such a change in a capacitance value is detectable using dedicated circuits designed in standard CMOS technology. As an example, in [**14**] capacitance variations lower than 1fF are revealed. It is just the set of sensing units that gives the name to the CoChiSe project, which is an acronym for Cell-on-Chip-bioSensor.

We have how it is critical to optimize sensing capabilities. The impedance variation depends both on the dimension of the well and on the properties of the used buffer. The typical dimension of a cell is around 10um, hence the well diameter and height need to be of the order of 100um.

There is more freedom about the choice of the solution, isotonic with the cell and able to sustain the cell functionality throughout the duration of the experiments, which last about tens of minutes. Also the position of the cells within the well affect the impedance measurements. In order to increase the detection capability, it will be important to control the cells position within the well.

To this aim each well will be equipped with a dielectrophoretic system to trap the cells in the region between the sensing electrodes. While dielectrophoretic forces are well known and widely used with single cells suspensions [**15**], it is also understood that an excessive use of it does damage cell living functions, critical for the CoChiSe project. In particular it would be optimal to perform the experiments in highly conductive buffers, which nonetheless implies local joule heating due to electrical currents.

Simulations demonstrated that the use of a custom and powerful refrigeration system is necessary to keep the temperature below 37°C, as required. Anyways the local temperature will not be controlled with a good resolution, due to the intense heating localized inside the wells, and the not-localized refrigeration. The purpose of the work proposed in this thesis is to use a different strategy to help dielectrophoretic forces to trap the cells at the centre of the wells.

1.3 Open microfluidic systems

Each well is filled up from a common reservoir at the bottom, from which the solution can be changed as desired. The cells are dispensed from an external ink-jet like nozzle, above the device (**Fig. 4**). Each well has an open extremity for the entrance of the cells. This open microfluidic network complicates the system with further concerns such as evaporation, contamination and control of environmental parameters required for cell cultures.

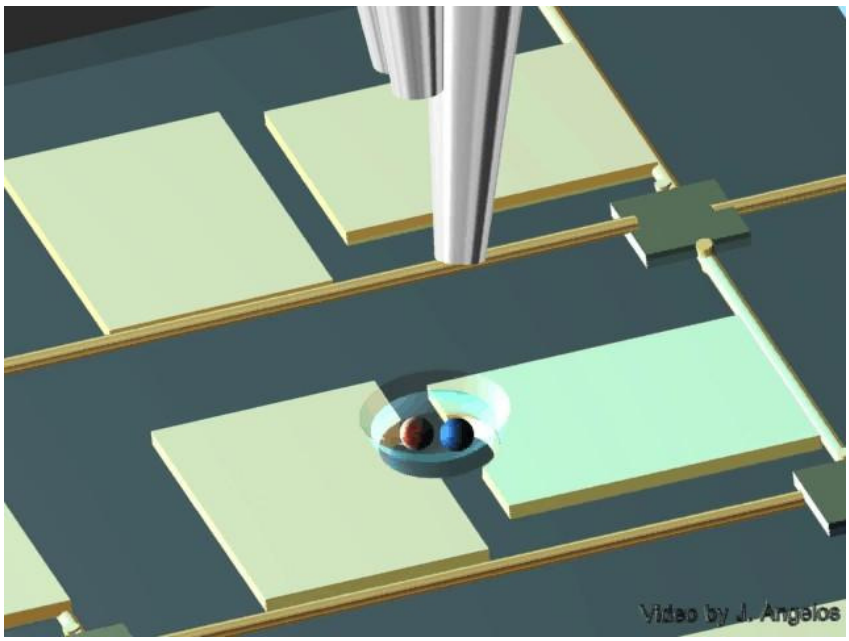

Fig. 4 The cells are dispensed from a nozzle above the micro-well array.

Evaporation is hence considered a negative characteristic in microfluidics, because the design of open microfluidic systems requires more attention to some details that are generally overlooked. Herein we describe a work performed to give more insight on the role of evaporation on the flow field.

2 Evaporative Flow Rate

Capillary forces drag fluids inside microchannels until the gravitational force and the capillary force match. If the channel has an open end, evaporation causes mass loss at the interface with air, therefore a fluid flow is induced to maintain the equilibrium condition. Particles suspended in the solution are dragged by the Stokes force along with the flow.

In this chapter we describe how this approach can be used to counteract the gravitational fall of cells in a culture medium and we propose a prototype used to determine the evaporative flow velocity through electronic impedance measurements. Optical inspection serves for a preliminary calibration step, after which the sensor is designed to work simply with electrical measurements. The data shown are obtained by using an aqueous solution at a controlled concentration of NaCl which is compatible with manipulation of particles of biological interest such as microbeads or liposomes, but the method can be easily extended for buffers compatible with living cells.

2.1 Working principle

2.1.1 Gravitational fall of cells

The principal forces acting on a particle suspended in a solution are: gravity, buoyancy, viscosity. Van der Waals forces are negligible far from the well surface, as well as Brownian motion due to the large dimension of cells.

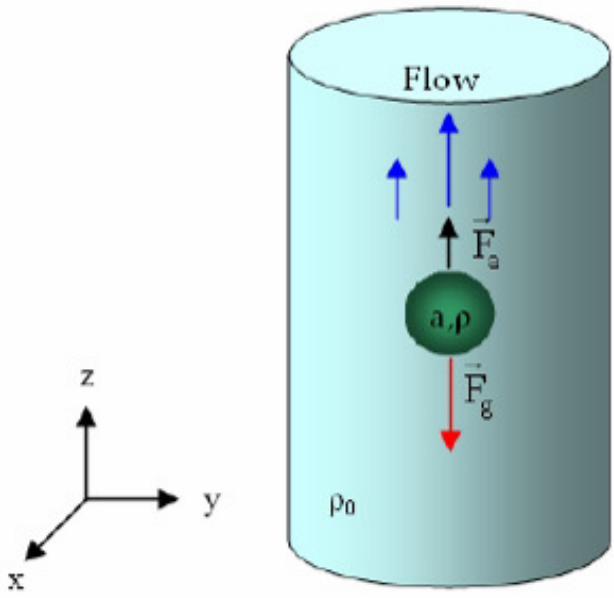

Fig. 5 Particle in a microfluidic channel and forces responsible for its motion.

Gravitational force with buoyancy and viscous forces are described as follows:

$$\vec{F}_{grav} = (\rho_{cell} - \rho_{sol})V_{cell}\vec{g} \sim \frac{4}{3}\pi(\rho_{cell} - \rho_{sol})a_{cell}^3\vec{g} \quad \textbf{(2.1)}$$

$$\vec{F}_{visc} = -k\vec{v} \sim -6\pi\eta_{sol}a_{cell}\vec{v} \quad \textbf{(2.2)}$$

where ρ_{cell}, ρ_{sol} are the mass densities of the cell and the solution, V_{cell}, a_{cell} the volume and radius of the cell, k, η_{sol} the stokes constant and viscosity of the solution, and $\vec{v}$ is the relative velocity of the cell respect to the surrounding medium.

To characterize the motion of the object in the fluid, it is helpful to define the Reynolds number $\Re$:

$$\Re = \frac{\lambda\rho_{sol}}{\eta_{sol}}\vec{v} \quad \textbf{(2.3)}$$

where λ is a characteristic dimension of the microfluidic system (a typical value used is the diameter of the cross section of the channel). When $\Re$ is small ($\Re << 2000$), the flow is essentially laminar. Systems such the ones used in the project are well in the laminar region, with λ~100um, $\vec{v}$~1um/s, σ_{sol}~1000Kg/m3, η_{sol}~10^{-3}Pa·s ($\Re$~10^{-1}). This results in a parabolic profile where the flow is completely developed. The absence of turbulences justifies the use of the Stokes law.

A third external force, dielectrophoresis, is used for the active control of the particles position:

$$\vec{F}_{DEP} = -\frac{\mathrm{Re}\,\tilde{\alpha}}{2}\vec{\nabla}\left|\vec{E}\right|^2 \quad \textbf{(2.4)}$$

where $\tilde{\alpha} = 3V_{cell}\,\varepsilon_0\varepsilon_{sol}\,\tilde{f}_{CM}$ and $\tilde{f}_{CM} = \frac{\tilde{\varepsilon}_{cell} - \tilde{\varepsilon}_{sol}}{\tilde{\varepsilon}_{cell} + 2\,\tilde{\varepsilon}_{sol}}$ is the complex Clausius-Mossotti factor in which

$\tilde{\varepsilon}_{sol} = \varepsilon_0 \varepsilon_{sol} - i\frac{\sigma_{sol}}{\omega}$ and $\tilde{\varepsilon}_{cell} = \varepsilon_0 \varepsilon_{cell} - i\frac{\sigma_{cell}}{\omega}$ are the complex dielectric constants of the medium and the cell respectively.

The dynamics of a cell in a flow is hence regulated by the equation:

$$m_{cell}\dot{\vec{v}} = -k\vec{v} + \vec{F}_{grav} + \vec{F}_{DEP} \qquad \textbf{(2.5)}$$

which solves to an exponential of time constant

$$\tau = \frac{m}{k} = \frac{2\rho_{cell}a_{cell}^2}{9\eta_{sol}} \sim 10^{-6}\,s \qquad \textbf{(2.6)}$$

The velocity is then practically always at the terminal velocity. In the absence of a dielectrophoretic force, the value of gravitational fall of a cell in solution is of the order of few micrometers per second:

$$\vec{v}_{term} = \frac{\vec{F}_{grav}}{6\pi\eta_{sol}a_{cell}} \sim 1\,\mu m/s \qquad \textbf{(2.7)}$$

2.1.2 Taking advantage of evaporation (to 1um/s, too)

The natural phenomenon at the basis of our theoretical approach of evaporation is plant leaf transpiration. A highly controlled experiment has been presented by Namasivayam et al. in 2003 [**16**]. Transpiration is the phenomenon that creates an upward flow of solution captured from the ground to bring nutrients up to the leaves. Water is lost due to evaporation, while surface tension at the leaf pores pulls more solution to

compensate for the lack of fluid in the capillaries. In [**16**] a mathematical model able to predict the evaporation from a highly controlled interface (Fig. 6) is described and experimentally proved.

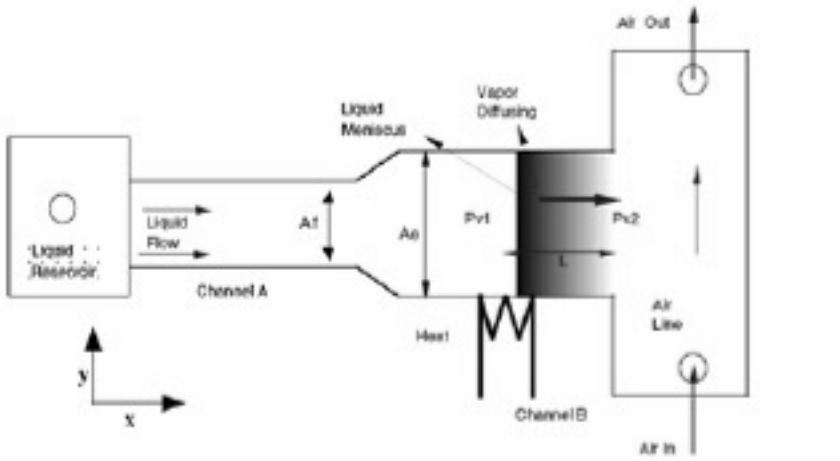

Fig. 6 Evaporation setup from Namasivayam: a microchannel is connected to an air inlet with known relative humidity.

The evaporation rate can be modelled with the following equation:

$$R_E = \frac{MA_E D}{RT}\left(\frac{P_{v1} - P_{v2}}{L}\right)\left(1 + \sqrt{\frac{u_0 W}{D}}\right) \qquad \textbf{(2.8)}$$

where M represents the molecular weight of water molecules, A_E the evaporation area, D the diffusivity of aqueous vapour, R the gas universal constant, T the absolute temperature, L the distance of the meniscus from the air channel, P_{v1} and P_{v2} respectively the saturation pressure of the vapour at the meniscus

interface and at a distance L from it, while u_0 is the air velocity and W the width of the meniscus.

Preliminary experiments (not shown herein) performed on the dimensions and geometry of the CoChiSe platform suggest that we can use the same formula for our system, considering an approximated L-value of 0.4mm [**17**], $u_0 = 0$, and using the room relative humidity for the calculations of the saturation pressures. The resulting flow is proportional to the meniscus surface area (the evaporation area). The main experimental parameter is then the average flow velocity, defined as the total flux divided by the cross section area. Both experimentally and theoretically, we obtain:

$$v_{avg} \sim 1\mu m / s \qquad \textbf{(2.9)}$$

an order of magnitude compatible with the gravitational fall of cells in solution (Eq.2.7).

The mathematical model used was designed for the setup described in Fig. 6. Our device is nonetheless substantially different: there is no direct control on vapour pressure at a defined distance from the meniscus, and the temperature is measured on the device surface, farther from the evaporation surface. In this way the evaporative process is way less controllable, but our setup is significantly simpler, and can be used for real-life biochips.

The work described above give both theoretical and experimental suggestion that the average evaporative flow velocity of a water-based solution (Eq.2.9) and the typical gravitational fall of cells (Eq.2.7) are of the same order of magnitude. Furthermore the two act on the cell in opposite directions.

What we have shown herein therefore suggests that evaporation could be an adequate pumping method to counteract the gravitational fall of cells in micro-devices.

2.1.3 Sensor operating principle (the 2 steps: Er and Z)

A schematic view of the meniscus sensor is sketched in Fig.1. The sensor consists of two electrodes located on top of an open micro-well to measure the impedance between them. A bottom metal layer acts as a ground plane. A micro-pump sets the fluid flow; depending on the micro-pump programming, a meniscus of different height *(h)* appears at the outlet of the micro-well.

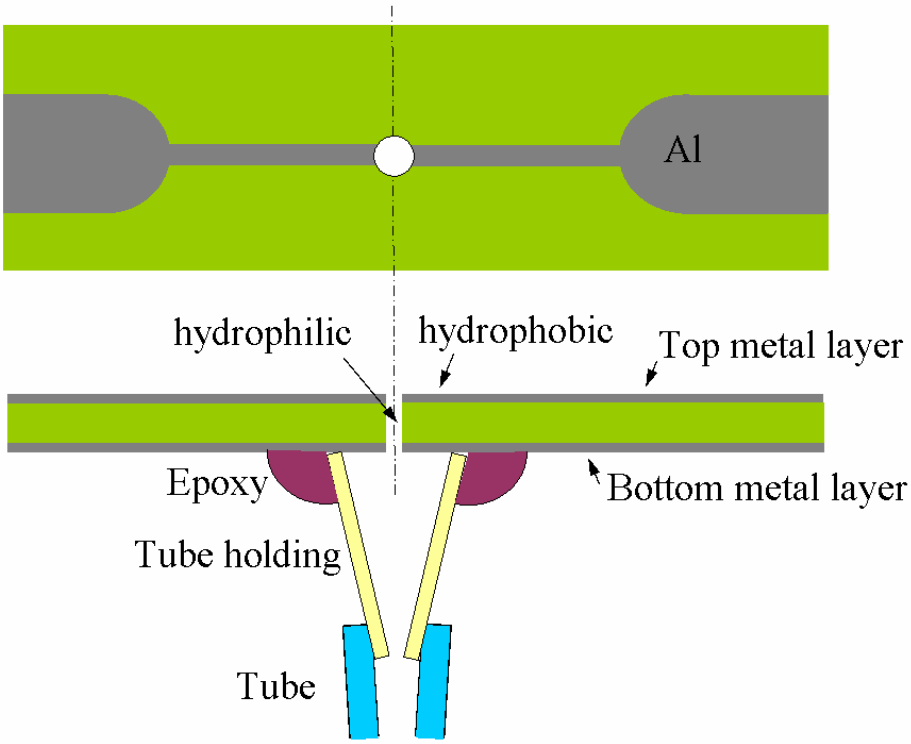

Fig. 7. Schematic view of the meniscus sensor

As an example, Fig. 8 shows a side view of the micro-well with a well-formed meniscus. The basic idea of this paper is that the impedance between the two electrodes is strongly correlated with the value of h, due to the large difference between the dielectric constant of the solution and that of air. We aim therefore to demonstrate that h can be measured through impedance sensing.

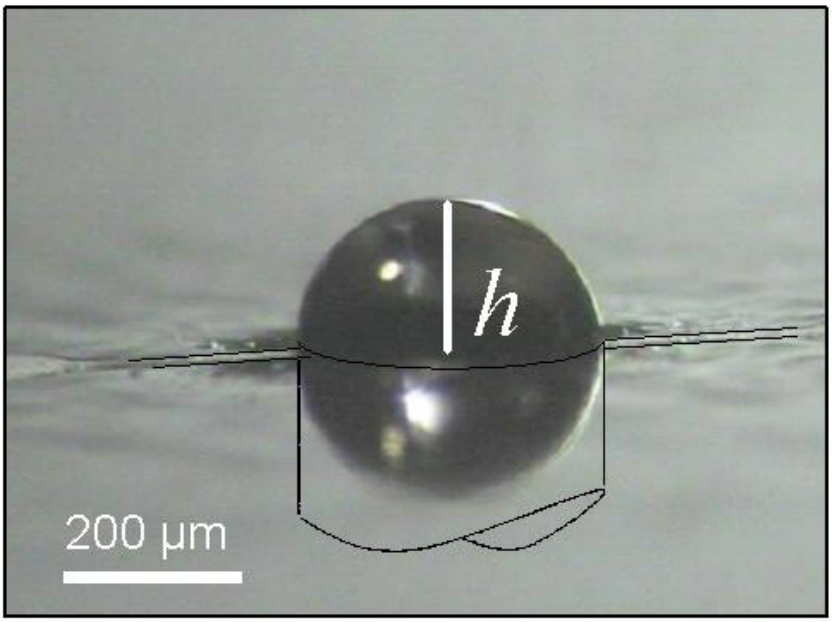

Fig. 8. Profile view of a micro-well. Meniscus height is shown at the exit of a microchannel. Electrodes for capacitive sensing of the meniscus height are visible in perspective on the sides of the droplet.

On the other hand, the rate (E_R) of the evaporative flow is proportional to the meniscus surface area, which is also related to h; a calibration step made through optical inspection allows one to find the relation between E_R and h. Merging this relationship with the sensor response through h allows us to find a correlation between the actual measured impedance and the evaporative flow rate.

2.2 Optical measurement

2.2.1 Transpiration pumps (to complete)

Fluid flow control through evaporation and capillarity has already been explored in the literature [**18**,**19**]. Previous work has used relatively complex approaches to measure the evaporative fluid flow [**16**,**20**]. These methods are difficult to use in applications where a multitude of open microfluidic structures are integrated. Other strategies have proved able to measure the very low fluid flow characteristic of the proposed device (below 1 µl/h) but they are either too complex [**21**] or require single-well inspection [**22**], making these methods unusable for micro-well arrays.

In this thesis we propose a system where the rate of flow induced by evaporation *(E_R)* is computed from the measurement of the meniscus height *(h)* at the outlet of a micro-well. Measurement of *h* is achieved by sensing the impedance between two electrodes located at the top of the micro-well. The sensor fabrication process and materials are compatible with future integration of the device in large arrays.

2.2.2 Evaporation Geometry

Typical dimensions of microfluidic devices range from a few micrometers to a millimetre. In this spectrum, the air-liquid interface is shaped by the surface tension, which is much larger than gravity. Surface tension leads to an approximately spherical shape of the meniscus surface. We use this approximation to set up an experimental strategy for measurement of the evaporative flow by optically measuring a single variable: the height of the meniscus *h*.

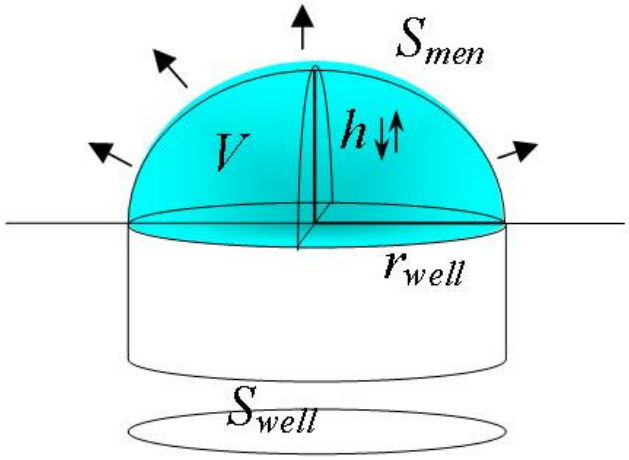

Fig. 9 Microwell sketch and definition of the meniscus geometrical parameters.

With reference to Fig. 9, the spherical approximation leads to the following geometrical relations between surface and volume of the meniscus region:

$$S_{men} = \pi r_{well}^2 \left(1 + \frac{h^2}{r_{well}^2}\right) = S_{well}\left(1 + \frac{h^2}{r_{well}^2}\right) \qquad \textbf{(2.10)}$$

$$\frac{dV}{dh} = \frac{1}{2} S_{men} \qquad \textbf{(2.11)}$$

where S_{men} is the meniscus surface, r_{well} the radius of the micro-well, h the meniscus height, S_{well} the section of the well and V the volume under the meniscus.

If the change in volume is due only to evaporation, and there is no flow injected by the micro-pump, the evaporative flow rate E_R is equal to the variation of liquid volume with time which, when combined with Eq (**2.11**), becomes:

$$E_R = \frac{dV}{dt} = \frac{dV}{dh}\frac{dh}{dt} = \frac{1}{2}\frac{dh}{dt} S_{men} \qquad \textbf{(2.12)}$$

2.2.3 Evaporation Curves

Under the approximation of uniform evaporation, the evaporative flow rate E_R and the evaporative surface S_{men} are proportional [**23**]:

$$E_R = \frac{k(T_{sol}, T_A, W_A)}{\rho}\left(x_A(T_A, RH) - x_{sat}(T_{sol})\right) S_{men} \qquad \textbf{(2.13)}$$

where ρ and k are the mass density and the mass diffusion coefficient of the solution, W_A the ventilation speed, and where x_A and x_{sat}, the humidity ratios, are functions of the relative humidity and air (T_A) and solution (T_{sol}) temperatures respectively.

Comparing Eq.(2.13) with Eq. (**2.12**), we expect *dh/dt* to be a constant depending only on the environmental parameters (*RH*, T_A, T_{sol}, and on ventilation) and on the solution properties (*k* and

ρ), but not on the diameter of the micro-well nor on the meniscus height.

Experiments were performed to optically measure h during evaporation in order to verify the expected linear relation between h and time. We set the experimental conditions to avoid refilling the evaporating solution from the meniscus: the pump was used to inject solution into the micro-well until the meniscus height was approximately a fourth of the diameter of the well. Then the flow was stopped to let the solution evaporate and lower the meniscus surface. Several evaporation runs were recorded and analyzed at T = 26ºC and RH = 33%, as shown in Fig. 10. The value of dh/dt is quantified through the angular coefficient of the linear regression of each evaporation curve, producing an average value of (1.05 ± 0.05) μm/s.

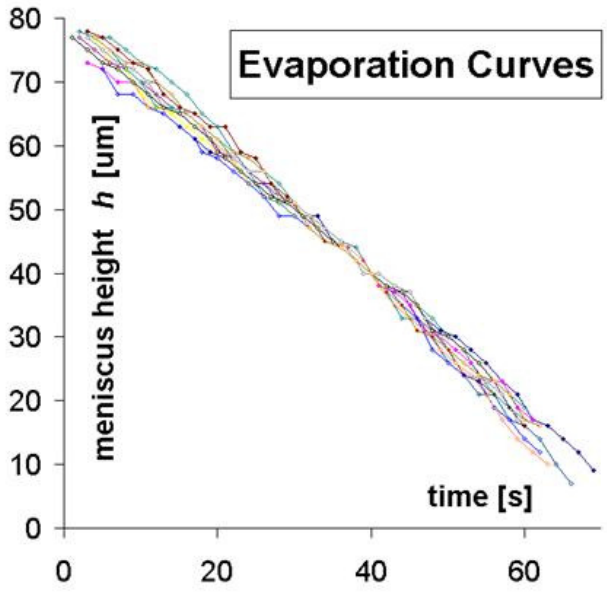

Fig. 10 Evaporation curves: meniscus height (h) versus time during 13 overlapped evaporation runs at T = 26 °C and RH

= 33%. A water solution with a controlled concentration of NaCl is used.

The linearity of the curves in Fig. 10 suggests that this method may be used for evaporation measurements. The evaporative flow rate can hence be computed through equations (**2.10**) and (**2.12**) as:

$$E_R = \frac{1}{2}\frac{dh}{dt}S_{men} = \frac{1}{2}\frac{dh}{dt}S_{well}\left(1+\frac{h^2}{r_{well}^2}\right) \qquad \textbf{(2.14)}$$

It is also possible to convert the evaporative flow rate of Eq. (2.14) to an average flow velocity by dividing the equation by S_{well} :

$$\langle v \rangle = \frac{1}{2}\frac{dh}{dt}\frac{S_{men}}{S_{well}} = \frac{1}{2}\frac{dh}{dt}\left(1+\frac{h^2}{r_{well}^2}\right) \qquad \textbf{(2.15)}$$

Substituting *dh/dt* by the experimental value deriving from Fig. 10, the average flow speed for $h = 0$ μm is (0.50 ± 0.03) μm/s. In particular, if h ranges from 0 μm to r_{well}, the average flow speed in the micro-well ranges from 0.5 to 1 μm/s at the environmental conditions described above.

2.2.4 Temperature dependence

The proposed evaporation experiment was repeated under different operating conditions (temperature and room relative humidity RH_{room}). The results are shown in Fig. 8, which reports the evaporation rate computed using Eq. (2.14) for $h = 0$ μm ($S_{well} = \pi \ r_{well}^2$, with $r_{well} = 170$ μm). Different sets of experiments performed on different days are represented on the

same graph. Temperature data are taken from the heating bath, while the temperature on the top surface of the device is less than 3°C colder than the heating bath temperature. Temperature 3 cm above the device ranges from 25°C to 30°C, increasing as the heating bath temperature raises. As expected an increase is observed in E_R with temperature.

For a constant temperature, the evaporation process is known to be proportional to the gradient of RH [**24**], which in turn is approximately proportional to the difference between RH at the meniscus (which is assumed 100%) and RH_{room} : $E_R \propto \nabla RH \approx \Delta RH = 100\% - RH_{room}$. In our experiments the room relative humidity varies in a limited range, from 24% to 37%, corresponding to a maximum relative variation in the evaporation rate of:

$$\frac{\Delta E_R}{E_{R,avg}} = 2\frac{(100\% - 24\%) - (100\% - 37\%)}{(100\% - 24\%) + (100\% - 37\%)} = 19\% \qquad \textbf{(2.16)}$$

On the other hand, the measurement uncertainty is about 25%, larger than the value in Eq. (2.16). Thus the effect of a variation in room relative humidity is hidden by the experimental uncertainty when observing a single data point.

However, it is possible to perform a statistical analysis of the two sets of measurements taken at similar temperatures (37°C and 38°C) and different RH_{room} (37% and 24% respectively) in order to observe a difference in sample averages. The null hypothesis that the two sets are not significantly different was rejected because its probability is lower than 2% (t-value=2.50), indicating that a statistical analysis recognizes a difference between the two sets of measurements. In particular, the experimental relative variation in average evaporation rate $(\overline{E}_R)$ is $\frac{\Delta \overline{E}_R}{\overline{E}_{R,avg}} = 2\frac{(0.324 - 0.271)}{(0.324 + 0.271)} = 18\%$, in good agreement with the value of 19% in Eq. 2.16.

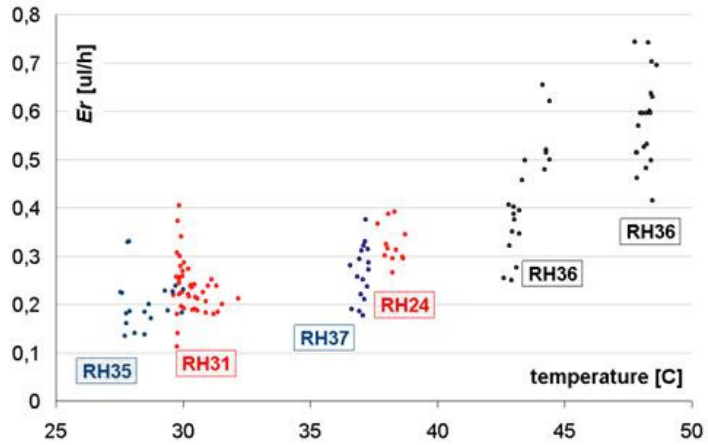

Fig. 11 Six sets of evaporative flow rates were computed as described in section 1.7 using Eq. 2.14 with h=0μm and the experimental *dh/dt* taken in different operating conditions. Data are represented as a function of temperature and are labelled with the environmental room relative humidity (RH). The average values of each sample and the standard deviation are shown with large dots and error-bars.

2.3 Electrical sensing

As we already stated, knowing the height of the meniscus at the top surface of the micro-well is important to perform a meaningful analysis of the average evaporation rate.

Using electrodes at the top edge of the well, it is possible to measure the impedance and know how much liquid and how much air is present between the electrodes. The order of magnitude of the capacitance measurements depends on the dimension of the well as well as the geometry of the electrodes.

In the next section, we will discuss a model for the evaluation of the order of magnitude of the capacitance in different geometrical conditions. This model will be the base of the calculations and data analysis performed in chapter 0. In section 2.3.2, an electrical model for the double layer capacitance is taken in consideration with the purpose of defining a good working frequency for the impedance measurements. Section 2.3.4 describes the experimental details, and section 2.3.5 the results.

2.3.1 Device technology

To design the measurement setup an anticipation of the typical value of capacitance measured is required. In particular, the microwells of the CoChiSe project are realized in a PCB which is composed of three metal layers separated by two dielectrics. The aspect ratio of the well is about one, where both the diameter and the height are around 100um.

While the inner part of the microchannel is naturally hydrophilic due to the fabrication process, the top surface is treated with spray PFTE to be hydrophobic. Once the device is in

contact with the buffer solution from the bottom, the solution climbs up the microwells and stops at the top surface. For this reason, the largest variation in capacitance is concentrated in the top part of the well, where a different meniscus height affects the space between the electrodes. The lower region is instead necessary to measure events inside the solution.

What expressed so far suggests to design the sensing electrodes in the top metal layer. A first prototype fabricated with an easier technology with only two metal layers is hence used for simplicity, instead of the three metal layers thought for the CoChiSe platform. Another difference with the planned device is that the prototype used for these experiments have larger wells, in the range 300-500um.

With this device it has been possible to evaluate a simple physical model of the measurement, and to prove the working principle of the evaporative flow rate meniscus sensor.

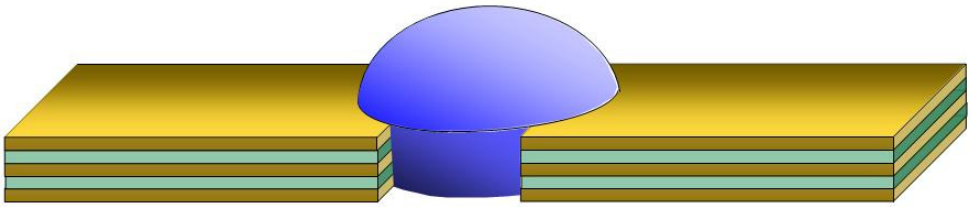

Fig. 12 Scheme of the micro-well thought for the CoChiSe project

2.3.2 Electrode pair model

A first estimate of the capacitive measurements can be obtained by combining the theory about coplanar electrodes with the one about parallel electrodes.

The electric field above and below the plane of the electrodes is elliptical, from the positive electrode to the negative one (Fig. 13). It can be modelled introducing two capacitances (C_{cop}) in parallel, representing the space above and below the top metal plane. If we imagine to have a couple of semi-infinite electrodes immersed in an homogeneous dielectric, separated by a distance $2a$, and forced at a potential $\pm V_0$, it is possible to obtain an analytical solution of the electrical field. The distribution of the bi-dimensional electric field can be resolved with the inverse cosine transform [**25**].

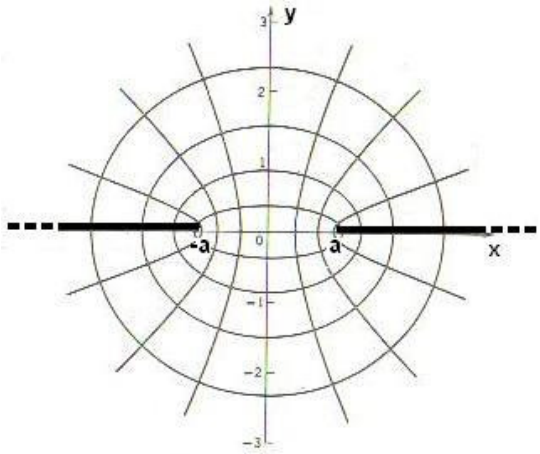

Fig. 13: Field lines between semi-infinite coplanar electrodes. The continuous lines represent the solution of the electric potential, the dashed lines represent the electrical flux.

This lets us calculate the surface charge on the electrodes:

$$C_{cop} = \frac{2\varepsilon_0 \varepsilon_r l}{\pi} \ln\left[\left(1+\frac{w}{a}\right)+\sqrt{\left(1+\frac{w}{a}\right)^2-1}\right] \qquad (\mathbf{2.17})$$

where w and l represent the length and width of the electrodes, a is the semi-distance between the electrodes, as shown in Fig. 14.

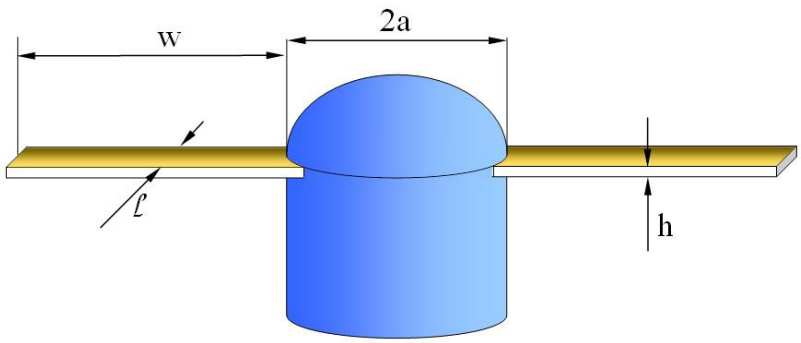

Fig. 14 First order model of the electrode geometry

The electric field in the region between the electrodes can be considered straight parallel to the electrodes in a first order approximation. This suggests to model this part with a standard parallel plate theory:

$$C_{par} = \varepsilon_0 \varepsilon_r \frac{lh}{2a} \qquad (\mathbf{2.18})$$

here h is the height of the metal layer, which is about 35um in the devices used. Even if it is clear that this is just a rough approximation because the electrodes facing the well are circularly shaped, and because $2a$ is larger than the other dimensions, it is possible to understand the influence of the region directly comprised between the electrodes on the capacitance measurements. The work is summarized in two Bachelor thesis [**26**,**27**], where the main conclusion is that the region directly between the electrodes plays a role in capacitance measurements. The scaling laws that will affect the measurements are also explained in the same thesis.

2.3.3 Double layer capacitance

Sensing capacitance measurements performed in microfluidic systems are affected by interface effects. They could invalidate the measurement and thus give us wrong information, mostly because we expect a low value of capacitance, according to the theory described in the former sections.

When electrodes are immersed in solution, at the metal-liquid interface the field-dependent concentration of solvated ions can be considered as a capacitance, commonly called double layer capacitance. Even when using the purest water solutions, in fact, we can find ions, due to the CO_2 absorption from the atmosphere, to diffusion from the solid phase and to ionization phenomena, for example. If the electrically charged electrodes are in a wet environment, the metal charge will attract the opposed charged ions that are dissolved in the liquid (see Fig. 15), while the molecules that have a dipole moment will align with the field.

The radius of the hydrated ions prevents direct contact between the metallic electrodes and the ions themselves. Furthermore, the ions diffusion causes a non-linear charge distribution: those two effects altogether are the main causes for the double layer capacitance.

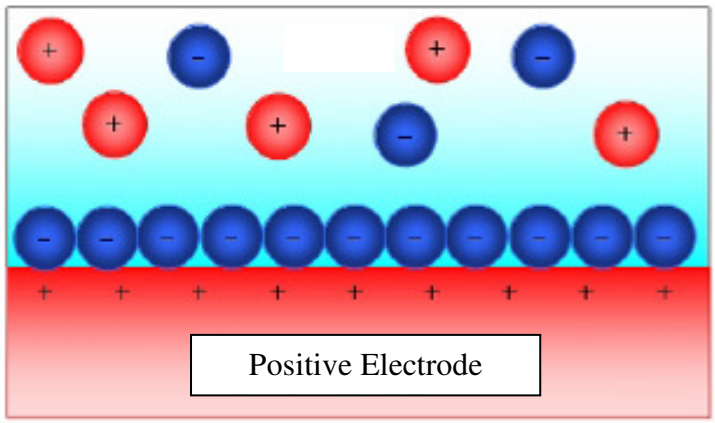

Fig. 15 Electric double layer

The charge distribution can be described by the *Gouy-Chapman* model, that considers two layers of charges: the *Stern's layer* and the *diffusive layer*. The charge of the ions in the Stern's layer is supposed to be concentrated at a distance of about 10Å from the electrode surface, set by the hydration radius. This layer can be modelled as a capacitance (C_{sterne}). In the case treated in this thesis, capacitance is about 20F/cm^2, regardless of ions concentration [**28**].

The diffusive layer, on the contrary, is due to the finite quantity of charge present in the Stern layer, and to the necessity of the double layer to be neutrally charged (see Fig. 16).

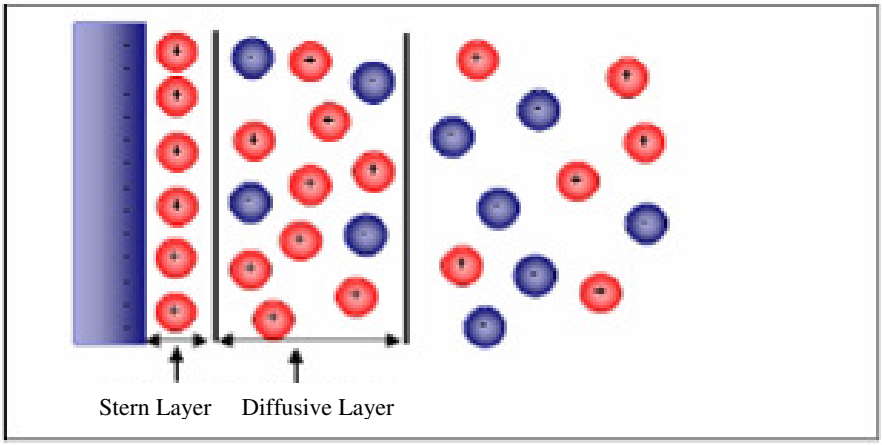

Fig. 16 Representation of the Stern layer and of the diffusive layer

The capacitance of the diffusive layer depends on its total thickness, function of the total concentration of ions. This thickness is called the *Debye's length*. The diffusive layer capacitance is the absolute dielectric constant divided by the Debye's length [28]:

$$C_{diff} = \varepsilon_0 \varepsilon_r k = \sqrt{\frac{2 \cdot 10^{-3} z^2 e^2 \varepsilon_0 \varepsilon_r C N_A}{k_B T}} \qquad (\mathbf{2.19})$$

where 1/k is the Debye length, z is the ions valence, e the electrons charge, C the concentration of ions, N_A the Avogadro number, and T the absolute temperature.

The equivalent electrical model of the solution between the electrodes, including the double layer capacitance and the bulk impedance is represented in Fig. 17. Here R_{sol} and C_{sol} represent the bulk resistance and capacitance respectively, while C_{DL} and Z_W represent the double layer capacitance and the Warburg impedance.

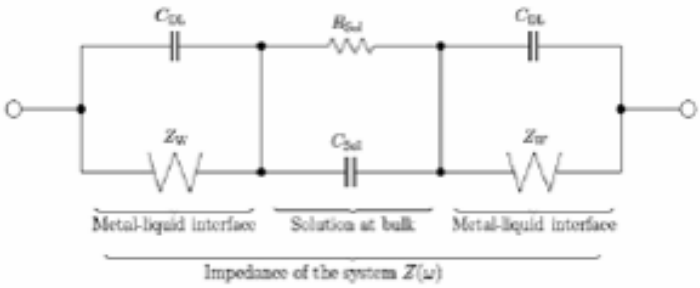

Fig. 17 Equivalent electric circuit of the metal-liquid interface and bulk

The Warburg impedance models the diffusive phenomena at the metal-liquid interface:

$$Z_W = \frac{\sigma}{\sqrt{2\omega}}(1-i) \qquad (\mathbf{2.20})$$

where σ depends on the bulk concentration and diffusion coefficients of the oxidant and the reducing agent, surface area of the electrode, number of electrons transferred and temperature.

Fig. 18 shows the ideal dependency on the frequency of the proposed model in a Nyquist diagram. The diagram is divided in two regions: at high frequencies the time constant of the solution

is dominant (the circular part in Fig. 18); at low frequencies a linear behaviour dependent on the impedance at the electrode interface.

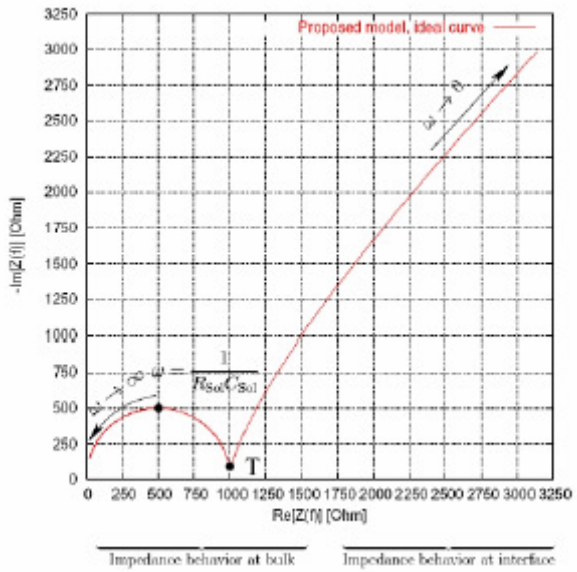

Fig. 18 Ideal Nyquist diagram of the model proposed in Fig. 17

For the purpose of sensing the meniscus height, which is the amount of solution contained between the electrodes, we are not interested in interface effects, so we want to work at high frequencies. Preliminary calculations show that the order of magnitude of the cut frequency is below 1MHz. The model proposed assumes that the medium between the electrodes is homogeneous, but in our case it is partly buffer and partly air. This introduces complications, such as a conductive layer at the meniscus surface, due to different surface effects, i.e. carbonation. For this reason the work we propose has been conducted at even higher frequencies: 10MHz.

2.3.4 Experimental setup

A demonstrator of the sensor is built using a novel technology for biomedical micro-devices [**29**,**30**] which is based on standard Printed Circuit Board (PCB) manufacturing thereby preserving the PCB characteristics of low production cost necessary for future integration of the proposed sensor into large arrays of microfluidic channels for parallel analysis. The fabrication process combines biocompatible dielectric materials layers, such as Pyralux and Polyimide, with Aluminium layers. Aluminium was chosen as the sensing metal because of its low-price, wide range of foil thicknesses and good electrical conductivity. It should also be noted that the thin layer of oxide that this metal creates when it comes in contact with air or water isolates the electrodes from the solution, minimizing Faradaic effects and corrosion. Aluminium was tested and validated for biocompatibility using cell lines involved in future applications of the sensor. The experimental protocol and the relative biological results are reported in [**30**].

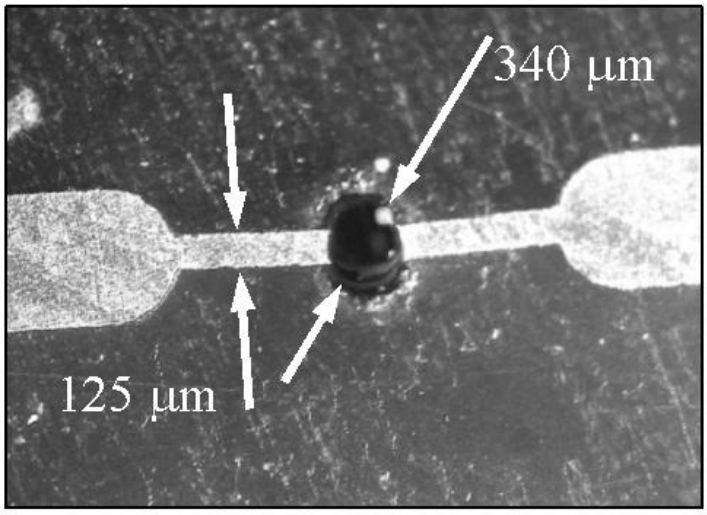

Fig. 19 Top view of a 340 μm diameter microwell.

The top layer houses the Al electrodes for sensing and the pads for contacting (Fig. 19). The two electrodes face the micro-well surface with an area of 125 μm (electrode width) by 18 μm (electrode thickness). Fig. 20 is a SEM image of a micro-well showing the stack of Al and dielectric layers. The bottom Al layer is a common ground plane. The multilayer is prepared by laminating two Al foils (18 μm) with two Polyimide foils (100 μm); Pyralux foils (DuPont, USA) are used as an adhesive, reaching a total thickness of 500 μm. The circuit is structured by laser, and covered with a hydrofluorocarbon (Certonal F732) to create a hydrophobic surface. The micro-wells are laser drilled to a diameter of 340 μm.

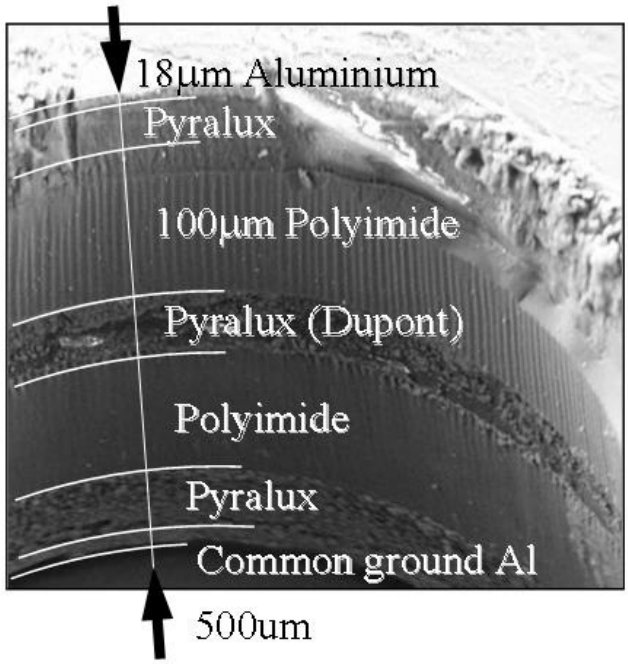

Fig. 20 SEM image of a microwell.

A water heating bath is set on the bottom Aluminium layer of the PCB to perform experiments at different temperatures. Two power resistances are used as heating elements, and the

temperature is measured through thermistors during experiments in 5 different locations around, on and inside the device. Silicone and teflon tubings are used as microfluidic interconnections.

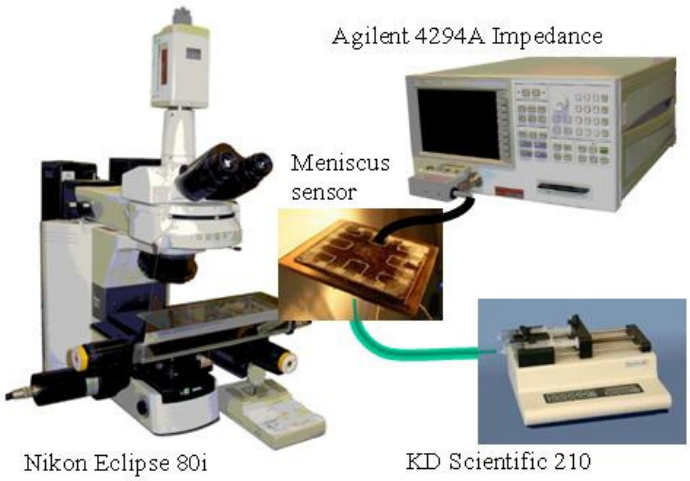

Fig. 21 Experimental setup.

The electronic, microfluidic and optical experimental setup is sketched in Fig. 21. The experiments were carried out using a calibration buffer of known conductivity (σ = 84 µS/cm) composed of NaCl < 0.01% in ultra-pure deionized water (Hanna Instruments). Impedance is measured with an Agilent 4294A Impedance Analyzer in the configuration with 4 terminals shielded, at room temperature (26°C) and average relative humidity 33%. The optical measurements are performed with a Nikon Eclipse80i microscope. Fluid flows are set by a KD Scientific 210 micro-pump and a Hamilton 250µl microsyringe.

2.3.5 Impedance measurements

As shown in Fig. 19, electrodes located at the top of the micro-well allow the electrical impedance between them to be measured. The value of the impedance is expected to be related to the meniscus height, due to the large difference between the dielectric constant of solution and air.

The measurements were carried out at 10 MHz, in order to remove the influence of the double layer impedance [**31**]. Compensation of the Impedance Analyzer instrument was performed on an empty well to remove the effects of stray capacitance. In this way, the value measured reflects only the variation of the impedance due to filling the well. The measurements are repeated for a meniscus height varying from 0 to approximately a fourth of the microwell diameter. Ten different sets of measurements were performed; the meniscus height versus resulting impedance module and phase is shown in Fig. 22 and Fig. 23 respectively.

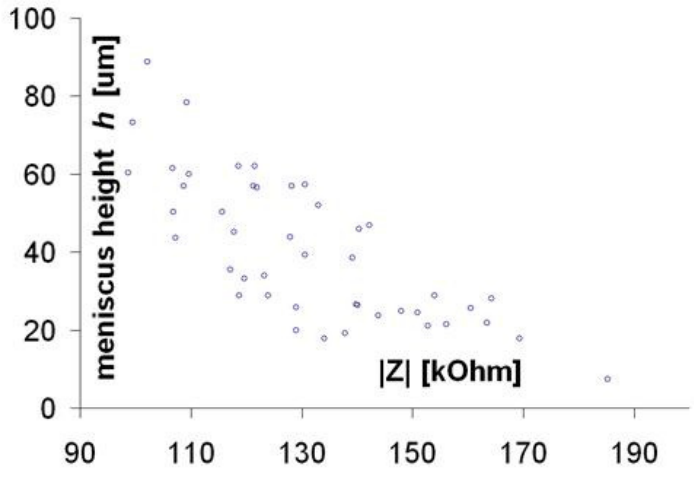

Fig. 22 Meniscus height versus module of the impedance between the electrodes.

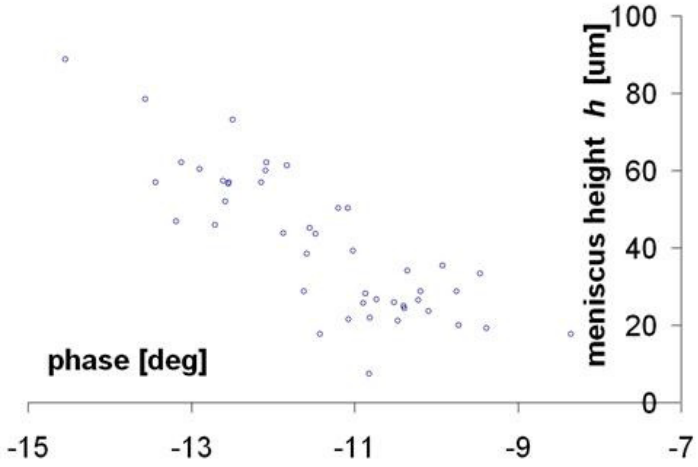

Fig. 23 Meniscus height versus phase of the impedance between the electrodes.

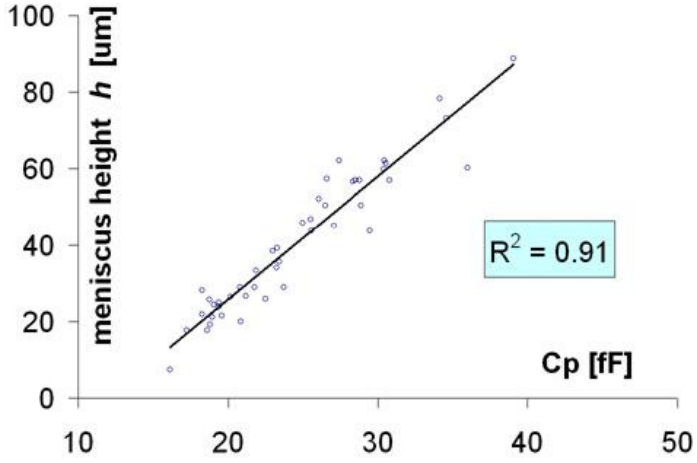

Fig. 24 Meniscus height versus capacitance value in the microwell of diameter = 340 µm shown in Fig. 19. Ten sets of measurements are represented. The linear correlation is demonstrated by the coefficient of determination $R^2 = 0.91$. Measurements were taken at 26 °C and RH = 33%.

We mapped the micro-well impedance into a simple RC parallel model. While the behaviour of C_P is approximately linear with h, as shown in Fig. 24, the resistive value R_P is almost quadratic and less reproducible (data not shown). It is possible that higher conductivity solutions could lead to an increase in resistive approach quality, which was here penalized by the low conductivity of the buffer used (σ = 84 µS/cm).

Linear regression was performed on the capacitance component in order to obtain the calibration curve that relates *Cp* with *h* (Fig. 24). The linearity of the fit is measured using the coefficient of determination R^2, which compares the variability of the estimation errors with the variability of the sample measured. The R^2 value is 0.91, which justifies the choice of a linear fit.

It is finally possible to convert the capacitive measurements in the evaporative flow rate using Eq. 2.14 and in the average flow velocity in the channel with Eq. 2.15 by substituting the experimental values of *dh/dt* and $h(C_P)$. Considering the value of *dh/dt* = (1.05 ± 0.05) µm/s from Fig. 10 and the relationship $h(C_P)$ from the graph in Fig. 24, we obtain the curve shown in Fig. 25, which is valid at T = 26 °C and RH = 33%.

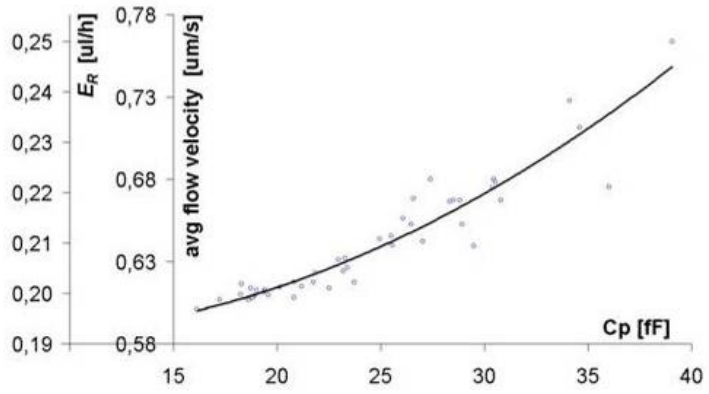

Fig. 25 Evaporation flow rate and average flow velocity induced in the microwell versus C_P at T = 26 °C and RH = 33%.

2.4 Summary

In this chapter we have presented a sensor which measures the meniscus height h at the outlet of an open micro-well in terms of the impedance between two electrodes located at the top of the micro-well. The sensor is built using a novel technology which preserves the low production cost characteristic of Printed Circuit Boards which is essential for any future integration of the proposed device into large arrays of microfluidic channels for parallel analysis. The diameter of the well is 340um. All the materials have been tested for biocompatibility. When one models the well by a simple parallel RC circuit, the experimental data show an approximately linear relationship between the meniscus height and the capacitance value. A calibration step based on optical inspection allows us to find a relationship between *h* and the evaporative flow rate**.** Combining through *h* the results of the optical calibration step and the electrical measurements, a correlation between the evaporative flow rate and the impedance value is finally found. Experimental data are taken using an aqueous solution with a controlled NaCl concentration; they show that the velocity of the fluid induced by evaporation ranges from 0.5 to 1µm/s when the meniscus height varies from 0 to approximately half of the well diameter. In our opinion, the experimental data discussed in this paper support the hypothesis that the evaporative flow could help to control the position of particles in an open micro-well, thus lowering the intensity of the electrical fields required for fine positioning.

3 Sensor Optimization

As observed in the previous chapter, the capacitance measured is of the order of few femtoFarads. Such a small value can be detected for example using dedicated circuits designed in a standard CMOS technology. The sensor is though thought to be part of a large array comprehending several thousand units, which severely complicates the detection system.

Effort has been put in the optimization of the sensor, mostly on the geometry of the electrodes and on the shielding against external interferences.

3.1Guarding electrodes

The equivalent electrical model used is described in chapter 2, section 2.3.2. The fabrication technology used for fast prototyping is a standard PCB photolithography of copper on fibreglass. The relative dielectric constant of the fibreglass is about 4, and the distance between the top and the bottom metal layers is 730um. In the previous chapter the metal used was aluminium, so that a layer of aluminium oxide creates as soon as the aluminium gets in contact with air or water. This isolates the electrode, thus preventing Faradaic currents. In the case of copper, the oxide forms as well, but is not able to isolate the metal, and keeps diffusing into the electrode. This risks to compromise the stability of the measurements. The microwells are obtained from the fibreglass by drill machining to a hole of 500um. The alternative strategy to isolate the electrodes is to spray PTFE on the top surface, while filling the microwells with a capillary, so that the inner part of the wells remains hydrophilic.

In the simplest electrode geometry, both the electrodes obtained from a single metal layer face the well, and all the field lines close from the positive electrode to the negative one, being attracted by the solution, which has a higher dielectric constant. In the electrode border regions, far from the well, the field lines are not influenced by the presence of the solution. In Fig. 26 a qualitative representation of the field lines is represented.

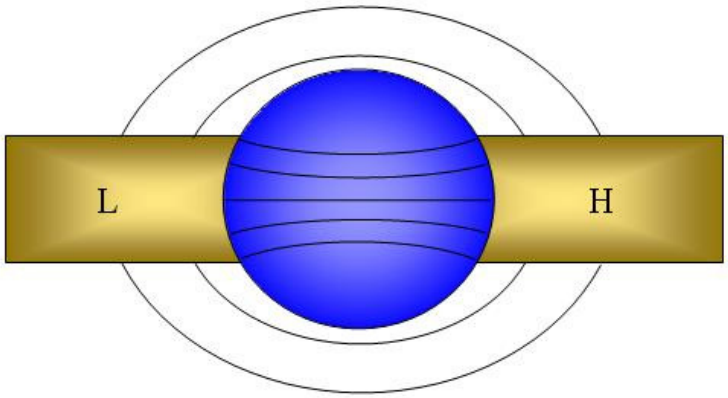

Fig. 26 Representation of the field lines between the electrodes in the configuration of a single electrode couple. L and H are the Low (virtual ground) and High (signal) terminal of the sensing instrument. The continuous lines qualitatively follow the field lines.

It is reasonable to represent the impedance between the electrodes as three capacitances in parallel, as shown in Fig. 27. Here C_{copl} and C_{par} are calculated by the model described in section 2.3.2, where the effective dielectric constants depend strongly on the presence of water in the well.

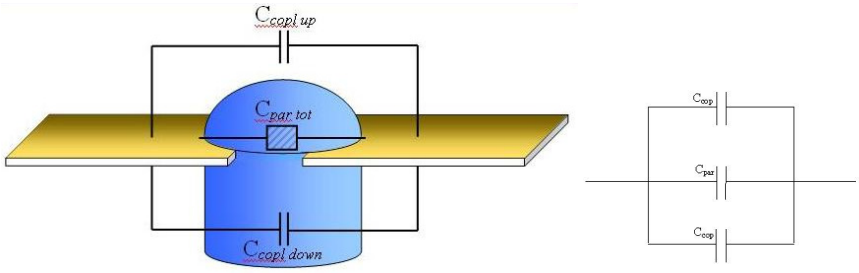

Fig. 27 First order model for the impedance between a single couple of electrodes

The results of the prediction of this theory are summarized in the next table:

		Capacitance below the top metal plane [fF]		Capacitance within the electrodes [fF]	Capacitance above the top metal plane [fF]	
l [um]	well state	min	max		min	max
100	empty	1.6	6.5	0.069	1.6	
	full	6.5	130	5.5	1.6	130
150	empty	2.4	9.8	0.10	2.44	
	full	9.8	195	8.3	2.4	195
200	empty	3.3	13	0.14	3.3	
	full	13	260	11	3.3	260
300	empty	4.9	19.5	0.21	4.9	
	full	19.5	391	17	4.9	391

Table 1

where *l* is the electrode width, and *h*=35um, *w*=1800um, *a*=225um

Different geometries could give easier measurements and a better resolution. The variables are: the width of the electrodes, which can be larger or smaller of the diameter of the well; metal

layers acting as shield ground electrodes; electrodes on the same metal plane of the sensing electrodes for shielding or guarding.

In the case in which the sensing electrodes are larger than the well, each of the three capacitances C_{copl_up}, C_{copl_down} and C_{par} can be divided into three capacitances in parallel, as shown in Fig. 28: the central portion is in fact strongly dependent on the presence of the solution, while the field lines connecting the two external regions are independent of it. In section 3.3.4 is shown how the external portion of the electrodes are responsible of a constant increase in the total measured capacitance.

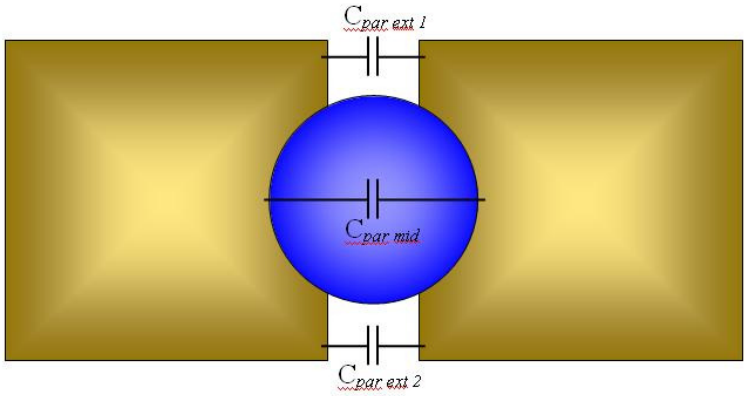

Fig. 28 Circuital model for a single electrode pair larger than the microwell diameter.

The shielding on the same metal plane of the sensing electrodes can be designed as a Faraday cage, shown in Fig. 29, where a single electrode is fabricated around the sensing ones. In this geometry, the external shield is grounded, while the sensing electrodes are posed at a virtual ground (L-electrode) and at a sinusoidal signal (H-electrode). This results in an asymmetric distribution of the electric field, where the field lines connect the signal electrode (H) to the other two. In Fig. 30 a qualitative view of the field lines is shown. To help comprehension, we should imagine the H-electrode surrounded by the other ones, so that the field lines come out of it radially, until closing to a grounded or virtually grounded electrode. The continuous lines connect the H

and L electrodes, and are responsible for the measurement. The dashed lines are not measured by the instrument.

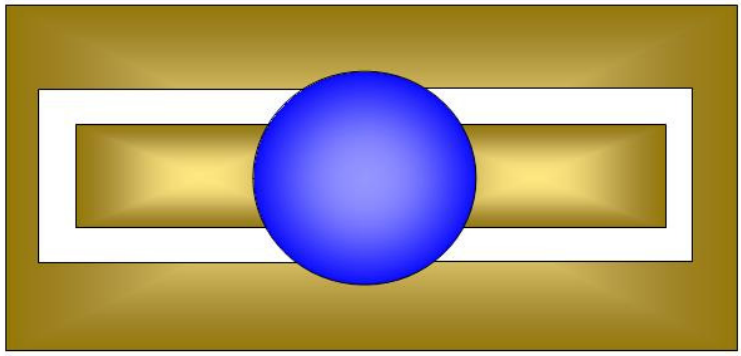

Fig. 29 Shielding electrode geometry

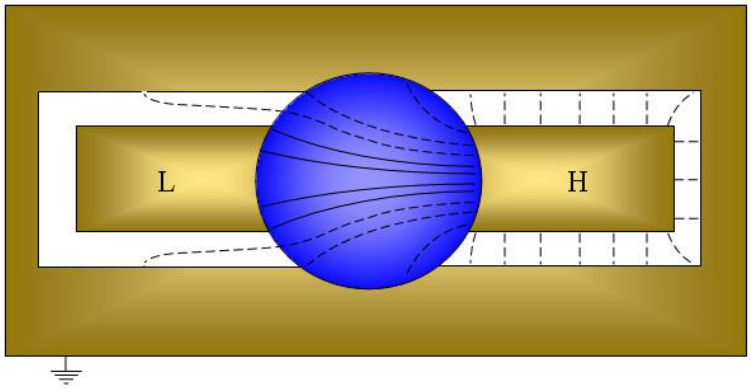

Fig. 30 Shielding electrode field lines. The continuous lines connect the two electrodes for sensing, and are responsible for the impedance measured.

This asymmetric distribution is not desirable, as it doesn't take in account the whole meniscus. The measurement would be more sensible to small changes localized in the central part of the meniscus close to the H-electrode, than on the corresponding region at the L-electrode.

An alternative to using shielding electrodes, is to design guarding electrodes, which are able to shape the electric field

lines as desired. If we divide the shielding electrode in two, we create the geometry of Fig. 31. The guarding principle is to exclude edge effects, so that the system is more similar to the predictive model. For this we need to surround the L-electrode with a grounded electrode, and to surround the H-electrode with a guarding electrode forced at the same potential.

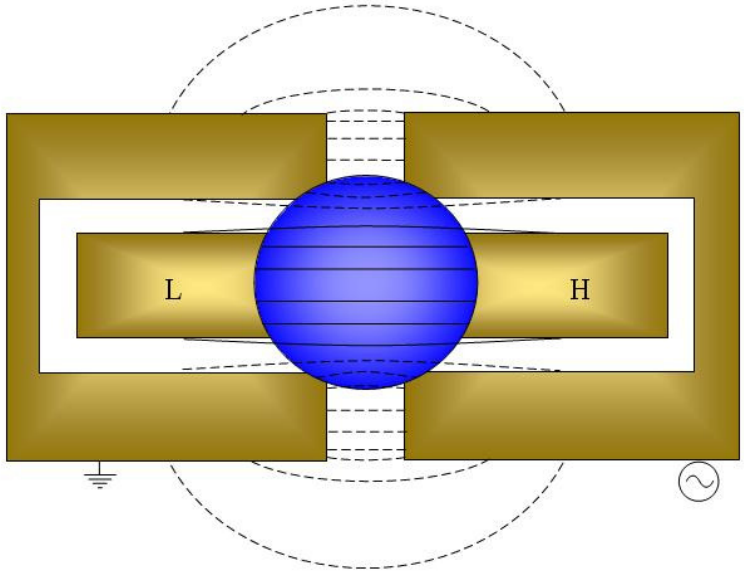

Fig. 31 Guarding electrodes geometry and field lines model. The continuous lines are responsible for the capacitance measured, while the dashed lines are not comprehended in the measurement.

In this way, the measurement is influenced only by the field lines in the region between the electrodes. Moreover the field lines connecting the two sensing electrodes are more straight, with less edge effects, which are only on the field lines from the guarding electrodes.

Unfortunately, forcing the signal potential to the guarding electrode without short-circuiting them is very difficult, so this interesting geometry is not very practical.

It is possible to practically implement the same idea developed for the guarding electrodes, but with a different geometry. The measuring system in fact sends a signal to the H-electrode, and measures the current passing through the L-electrode, which is at virtual ground thanks to an OpAmp. The impedance is then calculated by dividing the voltage phasor by the current phasor. With this setup, it is critical that the L-electrode is isolated by the rest, not to affect the current measured, but the H-electrode can be short-circuited to it's guarding electrode. The current passing through the H-electrode is then divided in two parts, one passing through the sensing electrode, and being measured; the other passing through the grounded electrode and not being measured.

The planned geometry is shown in Fig. 32.

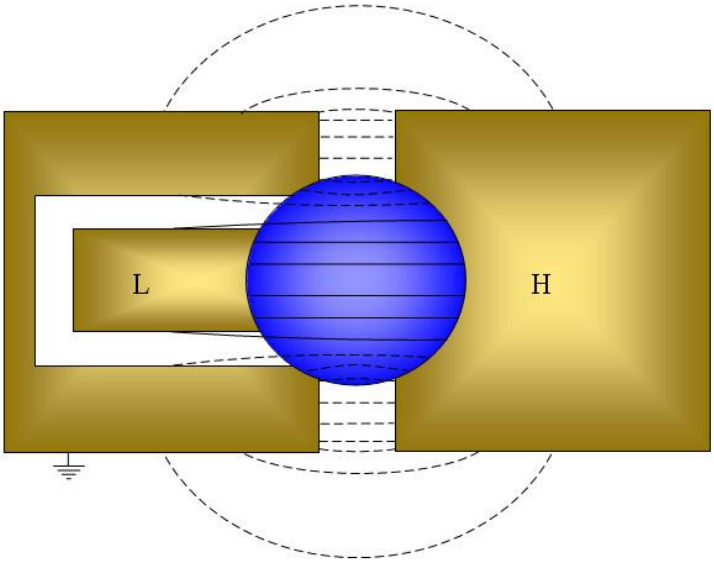

Fig. 32 Realizable guarding electrode geometry, with a grounded guard around the sensing electrode, and a larger signal electrode. Only the continuous field lines are the ones responsible for the impedance measurement.

The field lines are very similar to the ones of the geometry with two guarding electrodes, and the impedance measurement should

be the same. It is though much easier to realize the electrical connections.

3.2 Shielding electrodes

To the geometries described above, we can add another metal layer acting as a shielding electrode. The electric field varies as shown in Fig. 33.

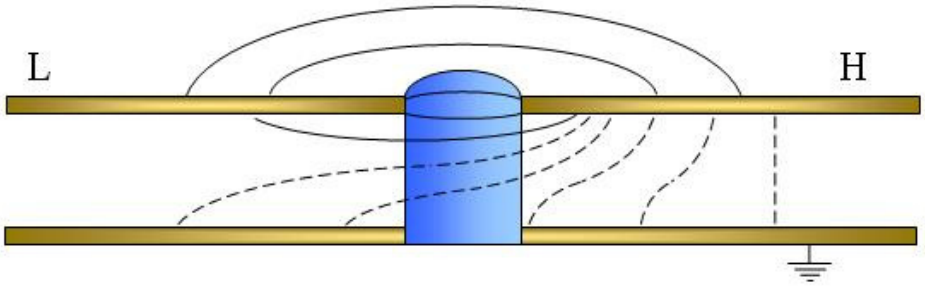

Fig. 33 Section of the bottom metal layer as ground shielding electrode. The field lines are shown. A common ground electrode on the bottom layer acts as a shield to exclude external interference from the measurements. The continuous lines are the ones measured. The dashed lines represent the field lines that are not comprehended in the measurement.

As in the previous case, the field lines connect the H-electrode with the other electrodes, so the field again is asymmetric. Contrarily with what said in the previous section, in which the asymmetry was unacceptable, in this case we believe that it won't be a problem, because we want to measure the variation of impedance in the region on top of the well, where is the meniscus.

The capacitance measure is supposed to be slightly lower than without the shield plane, because the bottom region of the channel

and of the dielectric is not comprehended in the measurements any more. Measurements performed without the shield electrode show interferences with the external world, such as the presence of the experimenter close to the device, while with this geometry they are more stable. We could think also of a more complex geometry, with the same perspective used in the previous section: we could divide the bottom metal layer in two parts, one below the forcing electrode, and the other below the sensing electrode and its guard (Fig. 34). This would further improve the symmetry of the setup, but would introduce a much more complex fabrication strategy, required for the alignment of the top metal layer with the bottom one. This would prevent the possibility of fast prototyping, and so decrease the potentiality of this approach.

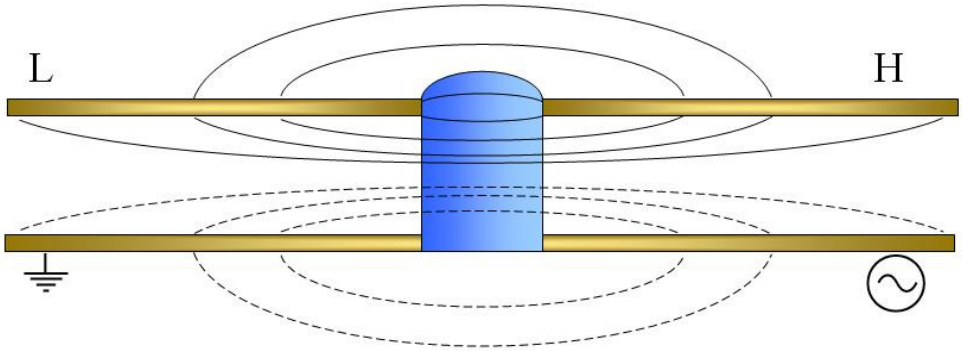

Fig. 34 Symmetric field lines in a geometry where the electrodes on the top metal layer are guarded by the bottom metal layer. The bottom layer is in fact divided in two parts, where the right one in the figure is short-circuited with the forcing electrode, and the left one is grounded.

3.3 Electrode width

In the previous chapter we have described that the optimal geometry for the electrical sensing is the one represented in Fig. 32, where on the top metal plane the sensing electrode is guarded by a grounded electrode, and the forcing electrode is much larger than the micro-well. The bottom metal layer is used as a shielding grounded electrode to minimize external interferences. It still unclear what would be the best width of the sensing electrode respect to the diameter of the well.

3.3.1 PCB design

The device used to determine the optimal width of the L-electrode, shown in Fig. 35, is fabricated with standard PCB technology [**32**]. A presensibilized board is exposed to UV light through a high optical density mask on the top metal layer. The photoresist is removed with NaOH 9g/l and the copper is removed in a $FeCl_3$ warm bath at 70°C. The residual photoresist is removed from the top and bottom metal layers with acetone. The micro-wells are drilled on the board with a 450um tip, without any particular aligning device, except for the eye of the experimenter. Optical mirrors are mounted on the sides, to allow for vertical optical access to the wells from the sides, in order to record and measure the height of the meniscus. Electrical SMD connectors are soldered from the bottom layer so that the ground plane is in solid contact with the guard of the connectors, and the central pin passes through the PCB to the top metal plane, where it is soldered with the electrode pad.

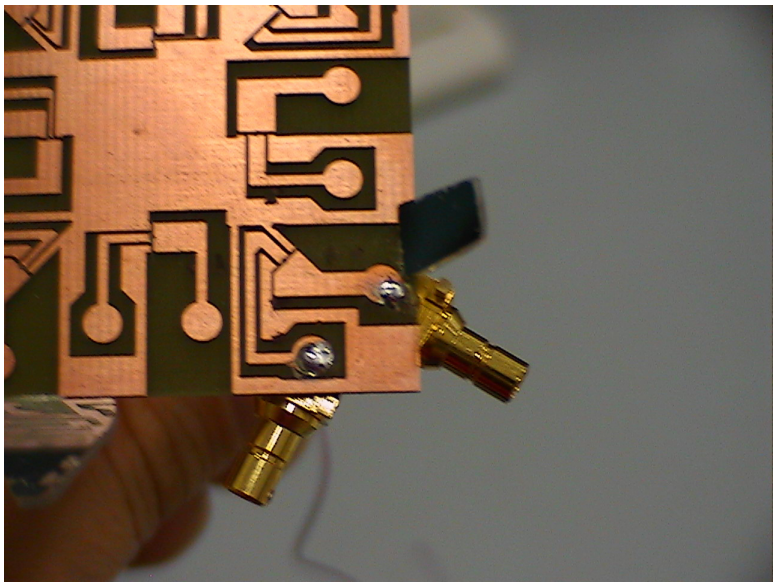

Fig. 35 Top view of the device used for the measurements that determine the optimal electrode geometry for the meniscus sensing.

Three wells have been chosen for the study, mostly due to the quality of the alignment. The geometrical dimensions are the same, except for the width of the sensing electrode, which is much smaller (130um), about the same dimension (397um) and larger (903um) than the well diameter(450um). The three electrodes are shown in Fig. 36, Fig. 37 and Fig. 38.

Fig. 36 Photograph of the micro-well with sensing electrode of 130um width

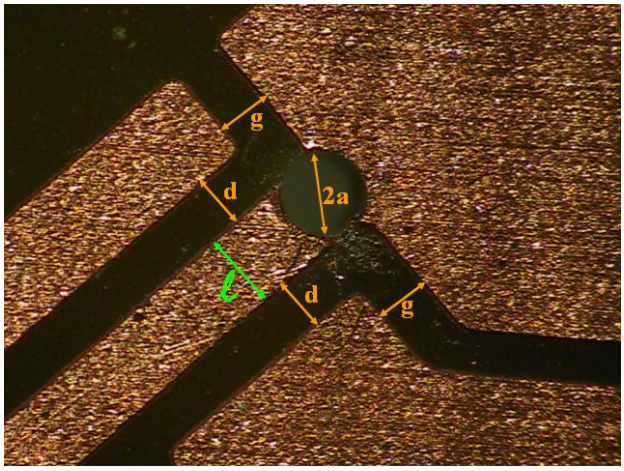

Fig. 37 Photograph of the micro-well with sensing electrode of 397um width

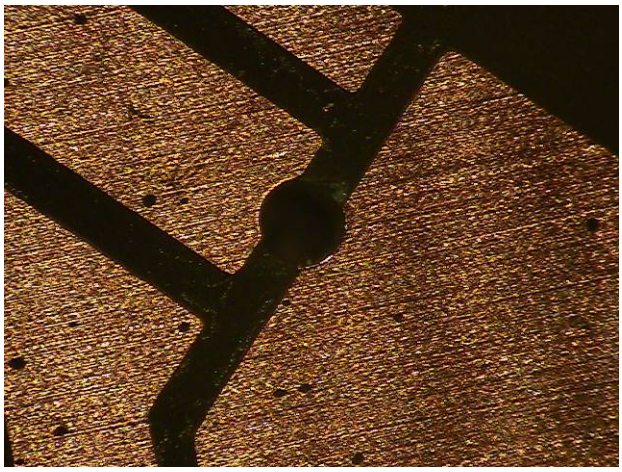

Fig. 38 Photograph of the micro-well with sensing electrode of 903um width

3.3.2 Empty well measurements

To evaluate if the physical model described above is correct, we verify that the capacitance measured when the micro-well is empty are in the same order of magnitude of the predictions. The signal is a sinusoidal with amplitude 250mV and frequency 10MHz.

The experimental results are shown in comparison with the minimum and maximum theoretical results in the following table [32]:

Electrode width [um]	Empty well capacitance [fF]	Min. predicted capacitance [fF]	Max. predicted capacitance [fF]
130	10.32 ± 0.02	4.3	10.7
397	17.77 ± 0.02	13.2	32.6
903	27.63 ± 0.02	62.1	84.1

Table 2

where the value reported for the empty well capacitance is an average value, and the uncertainty is calculated with the standard deviation of the population.

All the values measured are of the order of magnitude of the predicted values, and only the largest electrodes has a value outside of the predicted value. We shall remember now that the predictions don't mean to be precise, but to suggest an order of magnitude of the measurements.

3.3.3 Meniscus sensing

The injection control is performed through connectors similar to the ones described in the previous chapter. An infusion pump generates the flux desired by the user. The solution used is the same solution used in the previous chapter, with a well defined conductivity of 84uS/cm. The infusion pump allows us to fill the well with a controlled flux, and stop the flux when desired. After the formation of the meniscus, the flux is stopped. Without a refill, evaporation lowers the level of the meniscus, until it becomes flat. The infusion pump is then restarted for the next evaporating cycle. In this way, the meniscus height varies as in Fig. 39. The height of the meniscus optically measured is represented in the right y-axis, and is represented by triangles in the graph. In the same figure, the values of capacitance are shown with asterisks (right y-axis).

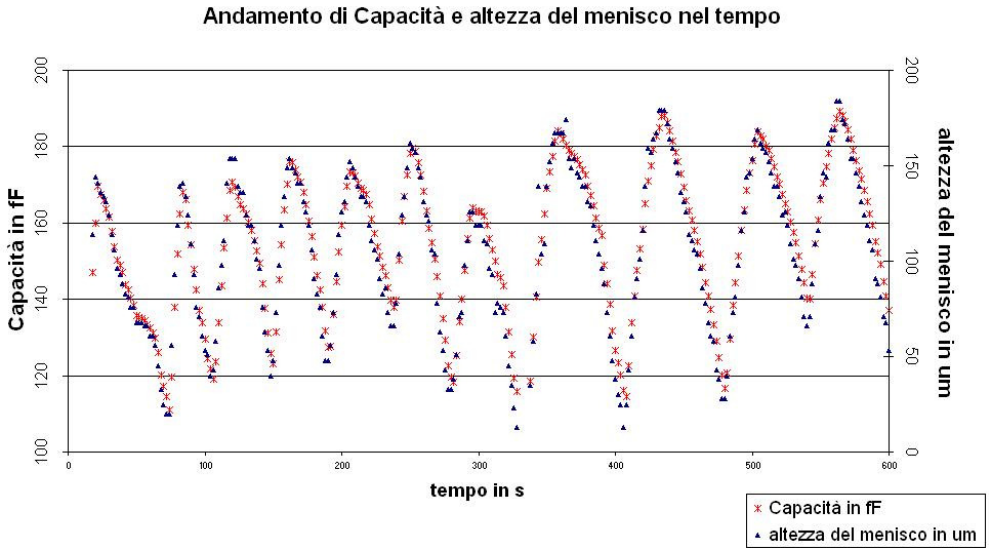

Fig. 39 Height of the meniscus vs time during several evaporation cycles. On the left y-axis, it is shown the measured capacitance (asterisks in the graph), and on the right y-axis there is the height of the meniscus respect to the top metal layer (triangles). The curves shown refer to the 397um well.

With this method it is possible to obtain measurements that correlate the meniscus height with the capacitance for a large range of meniscus heights. The results of several evaporation cycles are shown in Fig. 40, Fig. 41 and Fig. 42 [32].

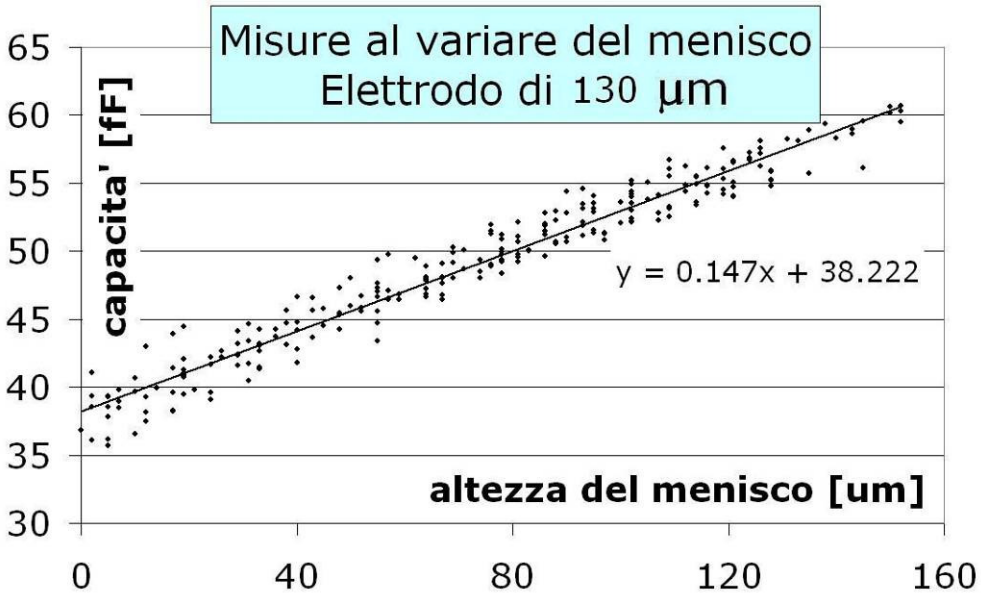

Fig. 40 Meniscus height capacitance sensing for the 130um well. The best fit line is represented and the formula for the fit is on the graph.

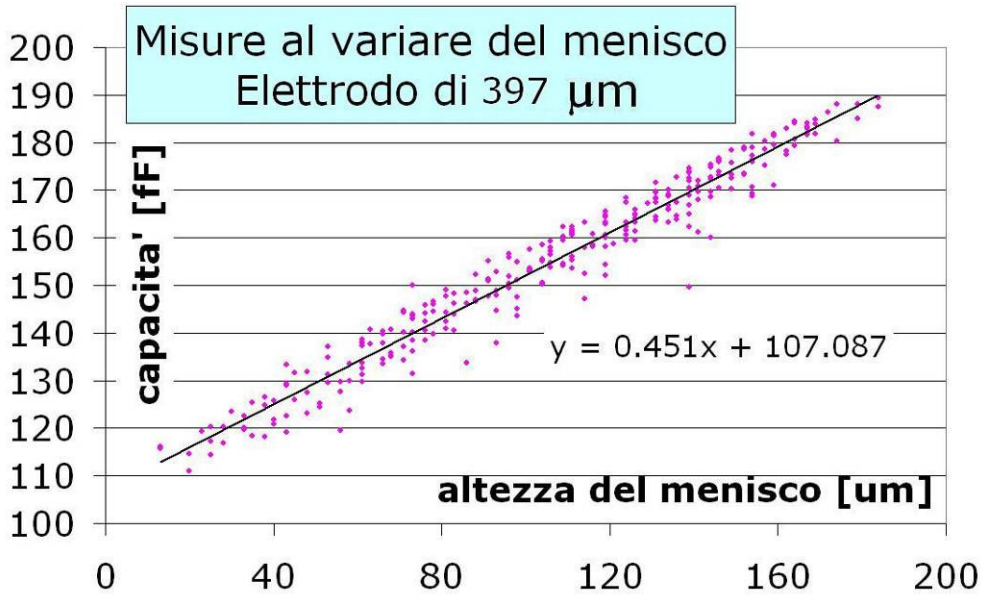

Fig. 41 Meniscus height capacitance sensing for the 390um well. The best fit line is represented and the formula for the fit is on the graph.

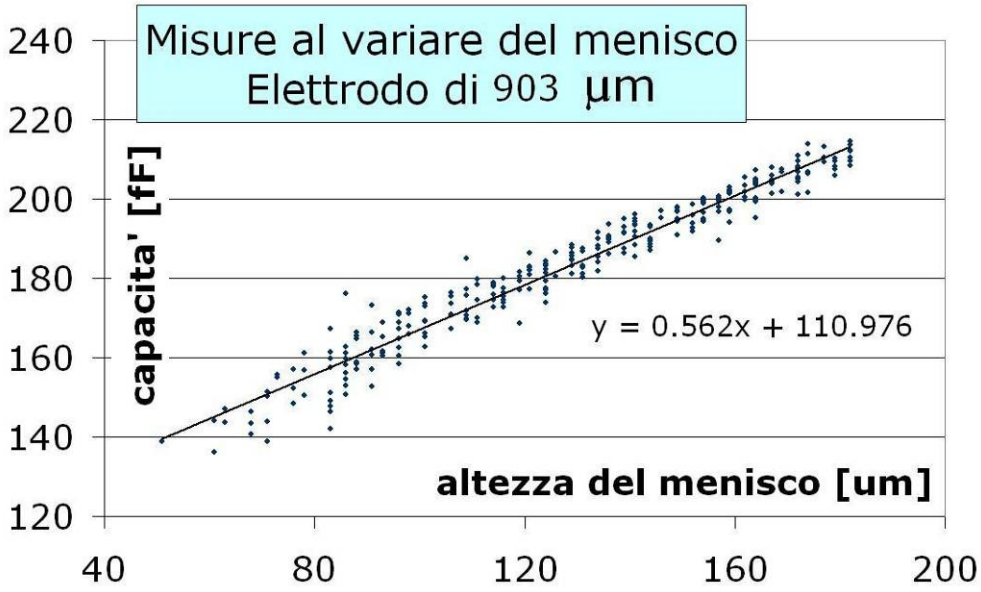

Fig. 42 Meniscus height capacitance sensing for the 903um well. The best fit line is represented and the formula for the fit is on the graph.

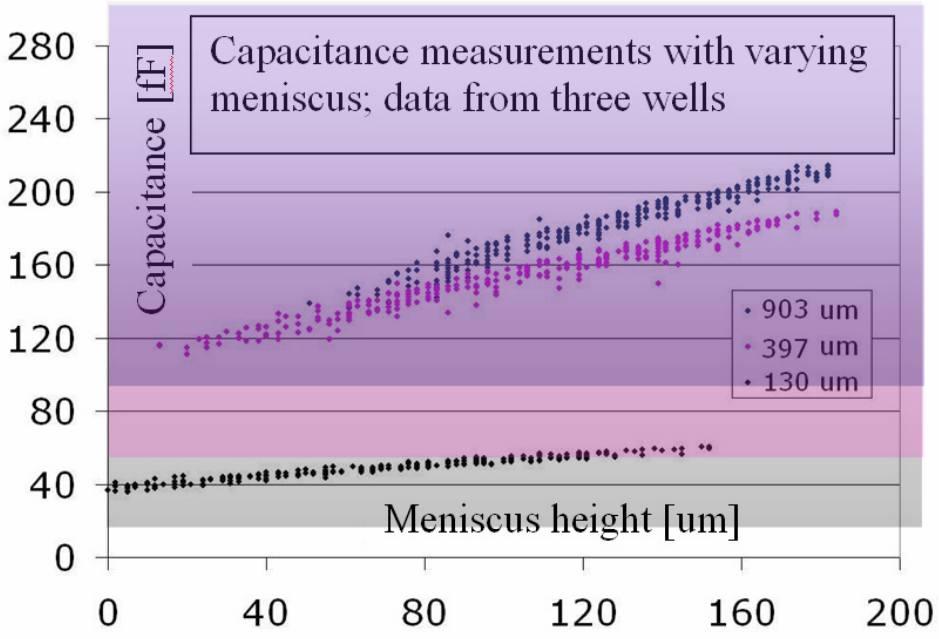

Fig. 43 Meniscus height capacitance sensing for the three electrode geometries in consideration. The theoretical expected ranges are highlighted in different colours. The experimental values lay within the expected range.

Electrode width [um]	Capacitance [fF]			
	Measured		Theoretical	
	min	max	min	max
130	35.7 ± 1.3	60.7 ± 1.3	17.7	346
397	111 ± 4	189 ± 4	54	1060
903	136 ±4	214 ± 4	109	1240

Table 3

In Fig. 43 and in the table above it is shown how all the measurements lay well within the expected ranges found from the theory of the previous sections.

In a similar manner as in the previous chapter, the three graphs show a linear dependence of capacitance versus height. The following table summarizes the results of the fit:

Electrode width [um]	Fit slope [pF/m]	Offset [fF]
130	147	38.222
397	451	107.087
903	562	110.976

Table 4

A correct analysis of the data requires to define the precision of the correlation between the capacitance value and the meniscus height in the three different cases. The measurements can then be compared and the best geometry can be chosen. The uncertainties related to the single measurements (both optical and electrical) can be neglected, as they are much smaller than the correlation uncertainty. The electrical uncertainty can be obtained by the measurements of empty wells. Its value is 0.02fF in all the setups. The optical uncertainty is dependent on the microscope used, and on the user, but is certainly of the order of few

micrometers. The distribution of the data points is also due to environmental factors, such as temperature and relative room humidity, physical factors, such as the condition of the electrodes, local salinity of the solution and presence of dirt at the meniscus.

The precision of the correlation cannot be defined by the uncertainty on the fitting parameters. If we consider the difference between the measured capacitance and its expected value for the fit (Fig. 44, Fig. 45 and Fig. 46), we can observe that the distribution is uniform while varying the meniscus height. It is hence possible to perform some one-dimensional statistics on these values. The standard deviation of the data is shown in Table 5, page 73.

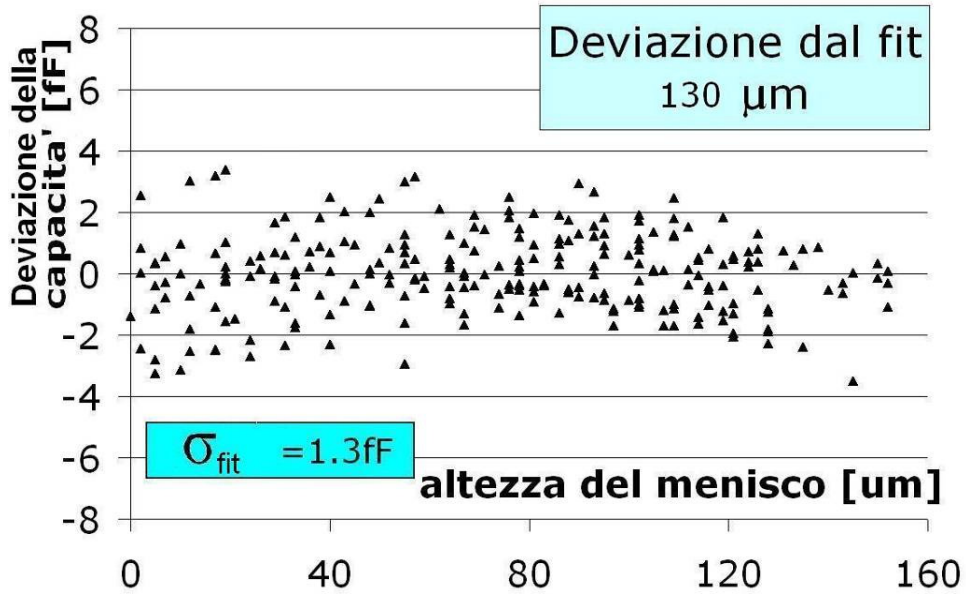

Fig. 44 Deviation of the capacitance measurements from the fit, for the 130um electrode.

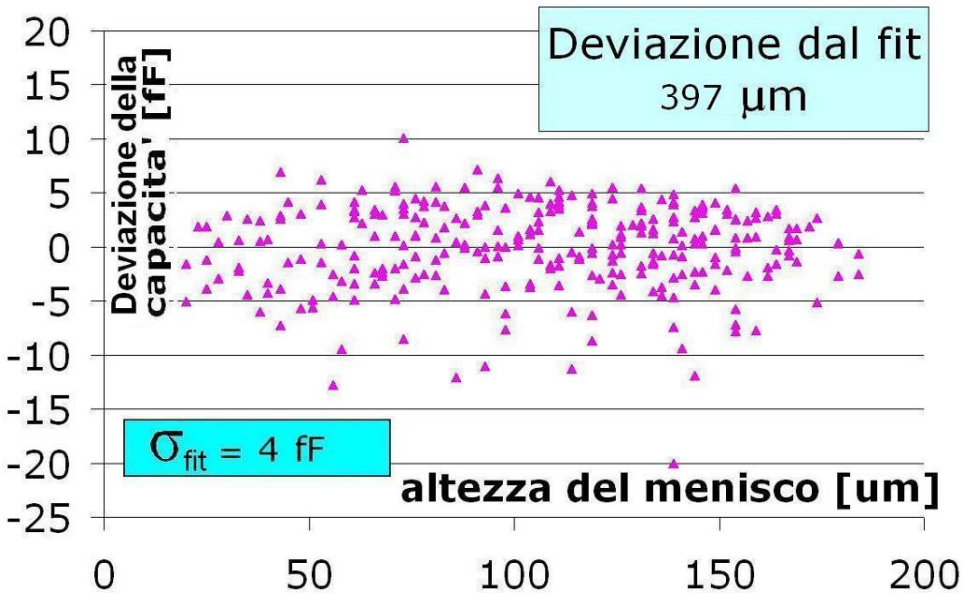

Fig. 45 Deviation of the capacitance measurements from the fit, for the 397um electrode.

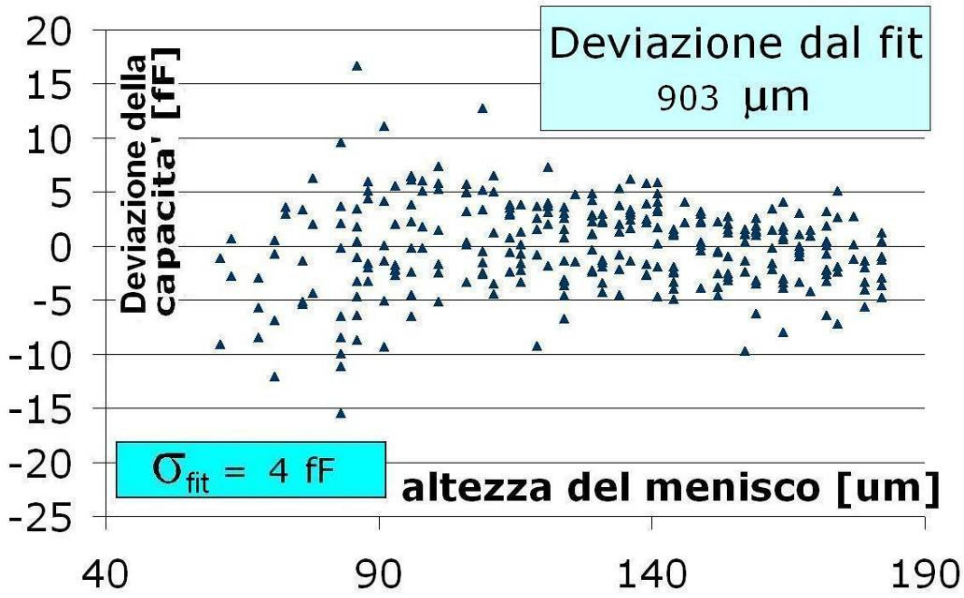

Fig. 46 Deviation of the capacitance measurements from the fit, for the 903um electrode.

3.3.4 Geometry comparison

To compare the measurements, it is optimal to observe them all in the same graph, in Fig. 47.

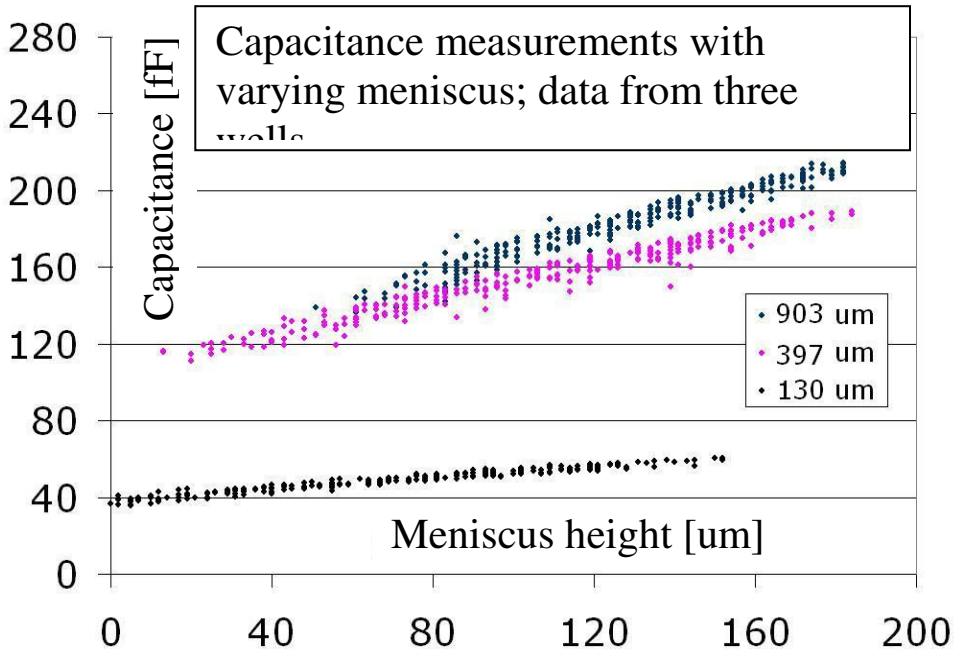

Fig. 47 Comparison of the three electrode geometries for capacitance sensing of the meniscus height.

Comparing the measurements made with the 130um and 397um electrodes, we need to take in consideration that larger electrodes generate larger currents. If we think at the field lines like in section 3.1, there is a larger number of field lines between larger electrodes. This variation is linear if the field lines are parallel, result obtained with the guarding electrodes, as explained at the end of section 3.1. This linearity reflects on the capacitance measured, so it is reasonable to believe that the measurement performed with the 397um electrode is larger than the other one by a factor 397/130. In this way it is possible to directly compare the curves, independently on the electrodes width.

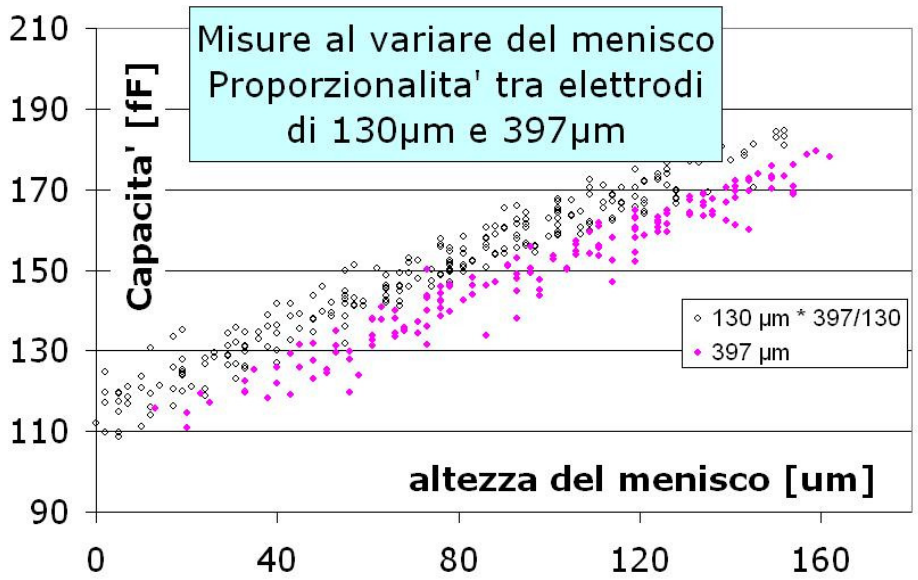

Fig. 48 The graph represent in fuchsia the data of the 397um electrode, and in black the data of the 130um electrode multiplied by 397/130. The data almost overlap.

This originates the graph in Fig. 48, where it is possible to see that there is an almost complete superposition of the data. Furthermore, all the fitting and statistics parameters get also multiplied by the same normalization constant 397/130. In this way the normalized parameters for the fit become practically equal for the 130um and the 397um data, as shown in the following table. Even more important than this, the standard deviations normalized also reach the same value. This concludes that the precision of the two electrodes geometry for capacitance-meniscus height correlation are practically equivalent.

Electrode width [um]	Fit slope [pF/m]	Offset [fF]	Std. deviation [fF]
130	147	38.222	1.3
130 normalized	449	116.724	4
397	451	107.087	4
903	562	110.976	4

Table 5

Given a value of meniscus height, the corresponding capacitance measurement has the same relative uncertainty with the two geometries. As an example we can take h=10um, then C=(40 ± 1.3)um using the 130um electrode, and C=(112 ± 4)um using the 397um electrode. The relative uncertainty of these values is respectively 3.2% and 3.6%, practically equivalent.

In the prototype under investigation, several electrical circuits will be present, some of which will be passed by the large currents needed for dielectrophoretic cell positioning. These will likely be sources of electrical interference. Thus the measurement of larger currents will be easier and more precise. This supports the choice of the 397um electrode versus the smaller one.

A different analysis is performed on the comparison between the 903um electrode and the 397um one. It is in fact clear that the normalization process could not help in this case. The theory of section 3.1 describes that we expect a constant increase in the capacitance measured. This can be observed in Fig. 47. Also the order of magnitude of the increase well fits with the theory. The similar shape of the data plot, along with the fact that the standard deviation respect to the fit assumes the same value of 4fF, suggests that the measurements are statistically very similar, and that both geometries can be used with different advantages: an electrode as large as the well is more difficult to align with the well during fabrication, but has the best relative uncertainty in the

capacitance-meniscus height correlation; a larger electrode is simpler to align and the measurement absolute uncertainty doesn't increase with the width.

3.4Summary

Different options for the sensing electrodes geometry is presented and modeled. In particular are taken in consideration different strategies for guarding and shielding the sensing electrodes. A geometrical design is chosen as the most promising, and it is built with standard fast prototyping PCB technology. The device, completed with specific optical and electrical access is tested to define the best value of electrode width.

The theoretical predictions obtained with a simple first order model have been confirmed by the measurements both in the presence and in the absence of solution in the well. Measurements have been taken at different meniscus heights for three different electrode widths: an electrode smaller than the well diameter (130um), one larger (903um) and another one approximately as large as the well.

As expected the curve related to the thinnest electrodes (130um) is approximately a third of the 397um one. The multiplicative factor can be related in particular to the ratio of the electrodes widths (103/397). On the contrary, the curve of the 903um electrode differs by the 397um one by a small constant, predicted by the theory. The different behavior can be explained by the particular guarding strategy used, designed to shape appropriately the electric field lines.

The results proposed in this chapter support the chosen strategy for guarding and shielding electrodes, in particular with electrodes of width comparable with the micro-well diameter or larger.

4 Convective Flow Patterns

While open microfluidics creates the transpiration effects quantified in the previous chapter, and simplifies the design of a biochip, it also presents several drawbacks, like the generation of complex evaporative flows at the interface. Being able to detect and measure these flows could allow to use them for controlling the position of particles inside microchannels.

Evaporation at the interface induces local flows due to the creation of a gradient in surface tension: the Marangoni effect.

Several experimental approaches have been used for measuring thermocapillary convection. Physical approaches measure the deflection of a probe such as a cantilever [**33**] to locally detect thermocapillary flows at a specific location. Currently the entire flow map can only be obtained through optical inspection. Optical approaches such as Particle Image Velocimetry (PIV) [37,38] and Particle Tracking Velocimetry (PTV) [39] image longitudinal sections of a microchannel containing micro-particles. The particles are dragged by the solution , so that the trace of the particles maps the thermocapillary flows along a section plane. Complete three-dimensional (3D) flow maps are obtained by stacking data from different sections [**34**].

We built a device in poly-di-methyl-syloxane composed of a vertical microchannel surrounded by a system of mirrors that let us track the 3D-position of single microbeads. With this system we are able to image the flows inside the channel, thus characterizing the Marangoni effect.

The experiments present a phenomenon where the geometrical symmetry of the device is broken and vortexes are created. The vortexes grow with time, until we are able to see only two columns of fluid flowing in opposite directions, one upwards and the other downwards. The generation of vortexes is reproducible, while the vortex rotational speed is dependent on the salinity of the solution used. The orientation of the vortex, though, is not reproducible.

The system is symmetric respect to the axis of the channel, hence suggesting the generation of symmetrical flow fields, such as the typical 3D toroidal vortex due to the Marangoni effect [**35**,**36**]. The convective flows are though asymmetric, with the generation of a single vortex.

We suggest that a possible cause for the broken symmetry is the local gradient in salt concentration due to inhomogeneous evaporation which, combined to the temperature gradient, makes the symmetric flow field unstable.

4.1Two-sided particle image velocimetry

The experiments for the investigation of the convective flows inside a microchannel are conducted on a custom device. A system of three mirrors is designed to get 3D information on the channel content, in particular to track single particles floating in the solution. Elaboration of the traces permits to reconstruct the particles trajectory, information that can be used to image the shape of the three-dimensional flow field.

While common comparable techniques (PIV [**37**,**38**] and PTV [**39**]) use microscopes with a thin focal plane optics, that image

slices of the channel, we use a large focal plane, small magnification stereomicroscope. Here lays the novelty in our approach: in this way we are able to observe the whole content of the channel, and obtain a complete image of single particles trajectories.

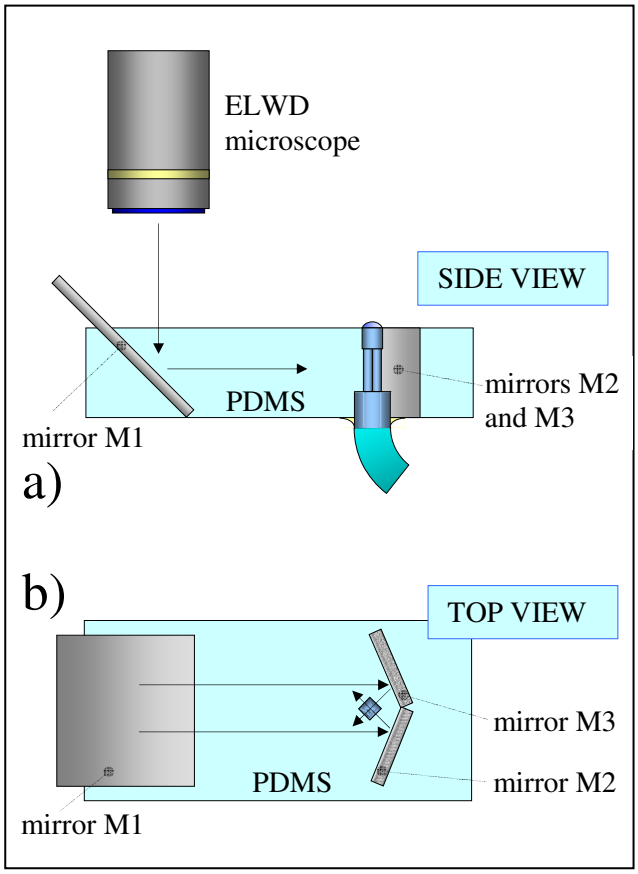

Fig. 49 Sketch of the microchannel with 3D optical access a) sideview b) topview

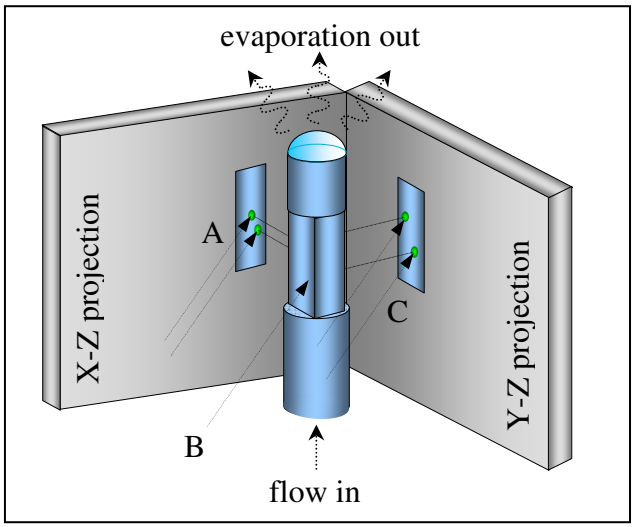

Fig. 50 The microchannel and the projecting mirrors in perspective.

The idea is to observe the channel from two different directions simultaneously. The two images can be used as two projections of the channel content and can be elaborated to reconstruct a whole 3D image.

The three mirrors are positioned to simplify the optical access: only one microscope and one acquisition system are required. A first mirror (M1 in Fig. 49a) is placed at 45° with the vertical, so that the optical path of the microscope is turned from vertical to horizontal. Two projecting mirrors (mirrors M2 and M3) are glued symmetrically at 67.5° (90°-22.5°) as shown in Fig. 49b. The disposition of the mirrors permits to two optical paths to reach the channel from two directions perpendicular to each other, thus allowing for simultaneous X-Z and Y-Z imaging. The two images can be reconstructed to a 3D XYZ image by comparison of the two Z information, as described in section 4.4.1. The arrangement of the projecting mirrors respect to the microfluidic channel is shown in perspective in Fig. 50.

In Fig. 50 it can also be observed that the region under investigation of the microchannel has a square section to minimize lens effects, while the rest of the channel is cylindrical.

During the experiments, a movie containing the two projections is recorded. The optical data is then elaborated to get a complete 4D information about space and time, which can be reconstructed to give both the position and the velocity of the particles.

A typical image viewed from the microscope is shown in Fig. 51. Three views of the microchannel are present: out of focus at the centre (B in Fig. 51) the channel is observed right after reflection from mirror M1; on its sides it is possible to observe the X-Z (A) and Y-Z (C) projections. The image shown in Fig. 51 is part of the movie elaborated to get the 3D tracks shown in Fig. 55.

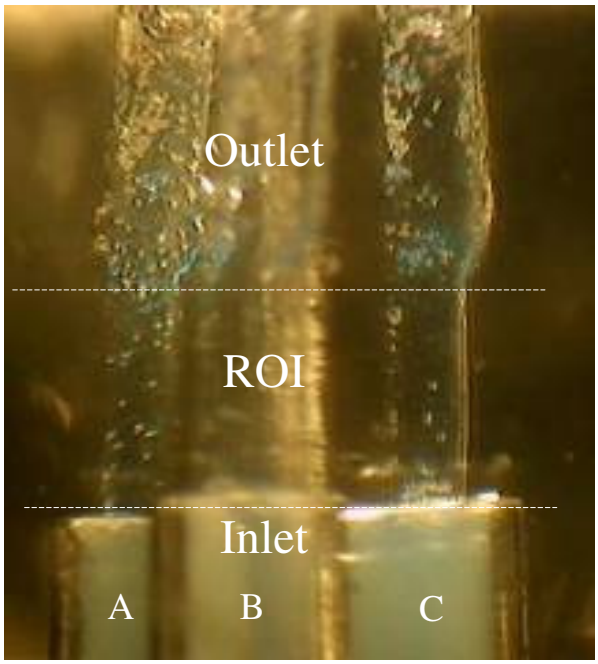

Fig. 51 View of the microwell from the microscope. On the left and right sides the two projections are visible.

4.2Device fabrication

The device comprehends a microchannel fabricated in Poly-d-Methyl-Syloxane (PDMS) and three mirrors around it, used for optical inspection (Fig. 52). The mirrors are embedded in PDMS and are oriented at the angles described in section 4.1. The fabrication steps used to build the device are described in the following list:

1) a hole is drilled on the bottom glass slide for the inlet;

2) the side glass walls and the mirror M1 are glued on the bottom glass slide. The mirror M1 is glued at 45° as shown in Fig. 49a;

3) the mould for the microchannel is composed of three sections: a square manually-polished metal pin of 400um side is glued between a 500um diameter glass capillary and a 1mm diameter PTFE tubing (Borland);

4) the two mirrors M2 and M3 and the microchannel mould are glued on the top glass slide using a very small amount of epoxy glue, to be able to remove the top glass slide after polymerization. The microchannel is oriented at 45° as shown in Fig. 49b;

5) PDMS (Sylgard 184 Dow Cornig) is prepared at the usual 1:10 proportions, mixed thoroughly, spinned at 2000 RPM for 2 minutes, poured in the mould and degassed for 30 minutes. The polymerization is conducted at 60 degrees overnight;

6) the glass lid and the microchannel mould are removed.

The microchannel mould is composed of three sections, as described above. The lower one, made from circular PTFE tubing is designed to host the microfluidic inlet. Sealing at the inlet is assured because the mould used for this part of the channel is the same tubing used for the inlet connection. The middle part corresponds to the region of interest, with a square section of

approximately 400um. A square section is used to avoid distortion due to lens effects. The top circular section is made of a glass capillary manually pulled from a Pasteur pipette. Its function is to end the channel with a circular opening, minimizing non-symmetric evaporative effects. The dimensions of the three parts of the microchannel are chosen in order to keep the section area as constant as possible: 500um inner diameter of the inlet connection tubing, 400um for the square section side, and 500um again for the outlet section. A sketch of the microchannel is shown in Fig. 50.

The device complies with the following characteristics: simple experimental setup, fast fabrication (about three days), low requirements for the instrumentation used for fabrication, flexibility in the design. The fabrication steps could be adapted for dimensions ranging from 100um to few millimetres and both for open or closed microchannels.

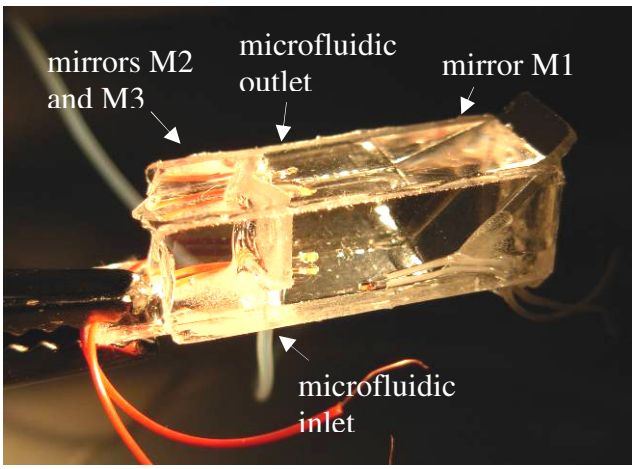

Fig. 52 Photograph of the device for 3D optical imaging of the convective flows.

4.3 Experimental method

4.3.1 Optical elaboration

The microchannel is observed through an upright Extra Long Working Distance stereomicroscope (Zeiss Stemi DV4) coupled to a commercial camcorder (Hitachi DZ-MV270 E PAL) recording at 15fps. Two external optical fibres illuminate the device.

The movie elaboration for tracking single particles is performed with VirtualDub and with a custom LabView software. A first elaboration is performed with a level filter and a motion blur filter on the single projections to obtain single images of the particles trace. A secondary, more time consuming elaboration is performed to record the three-dimensional position of single particles in time.

The projections of the particles positions are recorded separately on the playing movie. We used the Z-component of the 2D traces to understand which couple of X-Z and Y-Z belongs to the same particle. It is in fact expected that the plot of one Z-component versus the other shows a linear relation with angular coefficient 1 if the two 2D traces belong to the same particle. This analysis is better explained in section 4.4.1.

4.3.2 Communicant vessels

The solution is fed through a 50cm long silicone tubing of 500um inner diameter. The external reservoir is a 2ml Eppendorf tube hanging from a vertical column so that the user can adjust its height. Particular attention must be paid to avoid air bubbles while filling the tube. Once the desired height of the meniscus is reached, the reservoir is held stable to assure constant inlet

pressure. In all the experiments presented herein, the height of the reservoir is chosen so that the meniscus is held convex at the end of the channel.

The geometry of the mirrors allows also for inspection of the shape of the meniscus, both when it is concave or convex (Fig. 53). Once the desired height of the meniscus is reached, the height of the reservoir is held stable to assure constant inlet pressure. The following experiments refer to a convex meniscus of about 150um height.

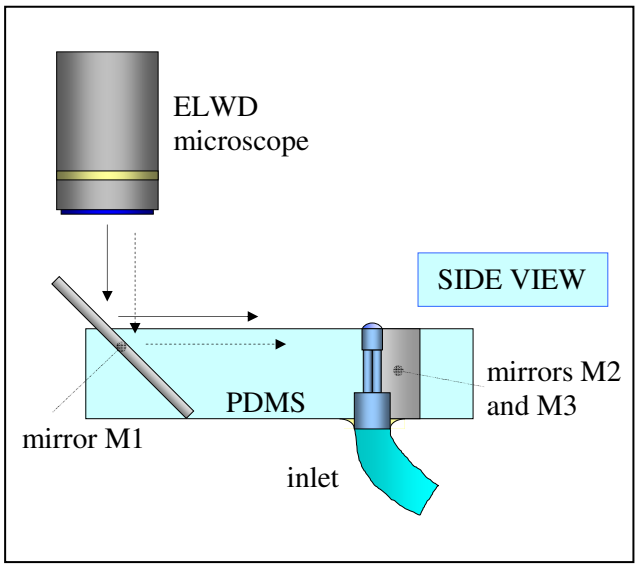

Fig. 53 Side view of the microfluidic device. The view of the meniscus height is possible both above and below the top surface.

4.3.3 Solutions and tracers

To observe variations in the vortex generation phenomenon due to salt concentration, we performed experiments in different water based solutions: Phosphate Buffer Saline (PBS), KCl 0.8M. The particles used are chosen so that their gravitational fall is

negligible with respect to the convective flows that we aim to characterize. We used 10um polystyrene beads for KCl 0.8M (the mass density is about 1.05Kg/dm^3 both for the beads and for the solution), and human leukemic K562 cells for PBS.

Under the action of only gravity and viscosity, the terminal velocity of a particle in solution is defined by eq. (2.6), and for water based solutions and particles of the order of 10um diameter, is of the order of 1us. We can hence consider that the particle stays always at its terminal velocity, which can be calculated as:

$$v_{term} = g\frac{m_{sol} - m_{part}}{6\pi\eta_{sol} a_{part}} = g\frac{2(\rho_{sol} - \rho_{part})a_{part}^2}{9\eta_{sol}} \qquad \textbf{(4.1)}$$

Where η_{sol} is the viscosity of the solution, a_{part} is the radius of the tracing particle, m_{sol}, m_{part}, ρ_{sol} and ρ_{part} are the inertial mass and mass density of the solution and the particle. It can be observed that the gravitational fall is proportional to a^2_{part} and to $\Delta\rho$.

We need the terminal velocity to be smaller than the a velocity related to the typical dimensions of our system: the height of the region of interest (about 1200um) divided by the maximum time for an experiment (30m). We hence want to be in the condition for which the terminal velocity due to gravitational fall is much smaller than 40um/s.

In order to obtain this value, we need to match the mass density of the solution with the mass density of the floating particles. For this reason a solution of KCl 0.8M (ρ_{sol_KCl}=1047kg/m^3) is used with 10um polystyrene microbeads (v_{term}~1um/s), while for PBS solution instead we use eukaryotic cells (cell line K562) (v_{term}~5um/s).

4.4 Vortex characterization

4.4.1 Three-dimensional particle tracking

Optical investigation covers a central part in this project. A custom software is used to analyze the movies recorded during the experiments. Each movie contains the two projections of the channel, hence contains all the information about the three-dimensional position of each suspended particle. The software gathers the position of the particles separately from each projection. The horizontal and vertical coordinates are called X and Z_x for the left side and Y and Z_y for the right side.

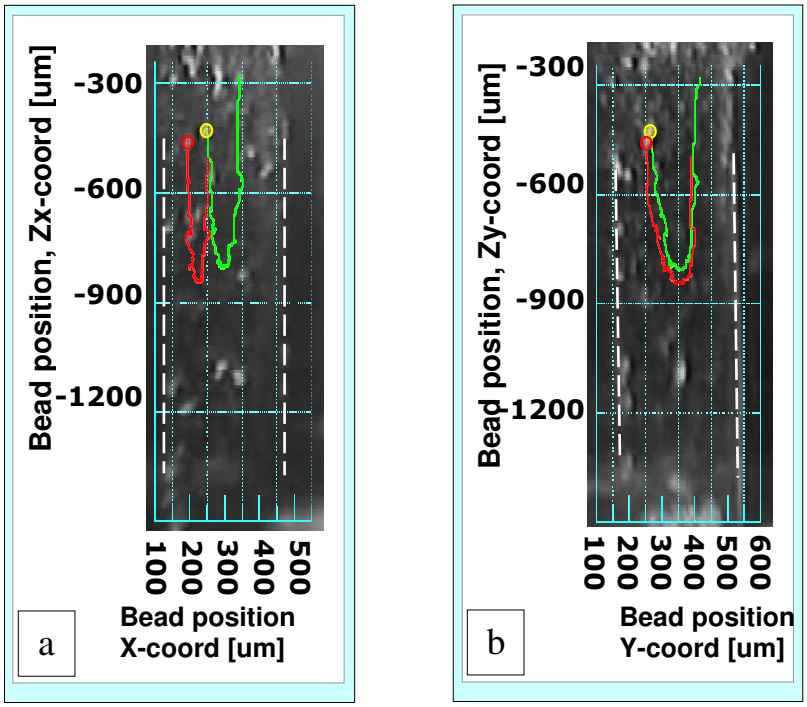

Fig. 54 The traces of two microbeads are superposed on the actual X-Z_x and Y-Z_y images of the channel.

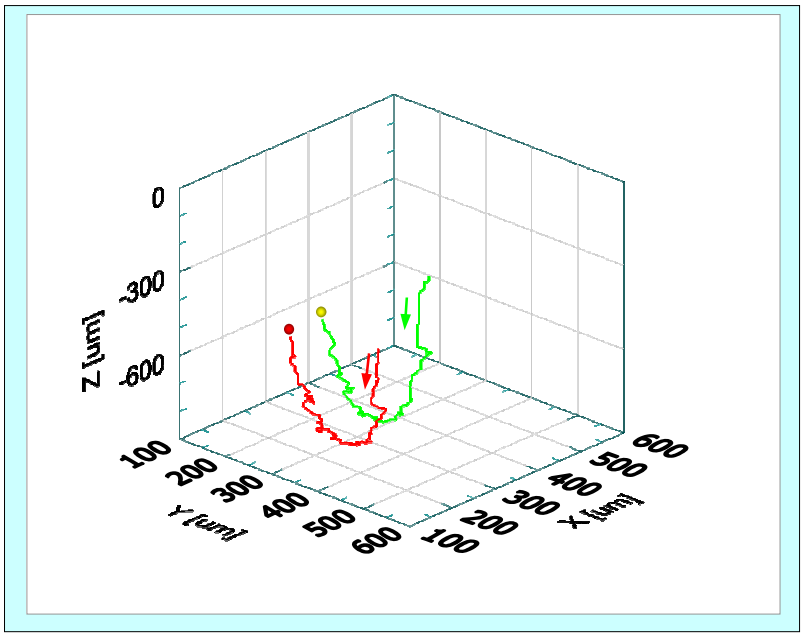

Fig. 55 Data from Fig. 54 is combined to form a three-dimensional reconstruction of the trajectory of the microbeads.

The X-Z_x and Y-Z_y tracks are recorded for different particles of interest. In Fig. 54a and b we show the tracks of two 10um microspheres in KCl 0.8M solution. For clarity the tracks are superimposed to a corresponding image of the channel taken from the movie. To reconstruct the 3D trajectory of single particles we need to associate each X-Z_x track with the corresponding Y-Z_y track. Considering that both the Z_x and Z_y coordinates associated to a single particle refer to the particle's height, this is performed by selecting the most linear Z_x-Z_y plot with angular coefficient equal to 1. Each point of a track is then defined with the coordinates $(X,Y,½(Z_x+Z_y))$. In Fig. 55 a perspective of the 3D reconstruction of the tracks of Fig. 54 is shown.

The time information can be added to the space coordinates in order to calculate the particle velocity. Associating to each point

the time *t* of the frame in which the space coordinates were measured, a track is thus defined in space and time with the coordinates $(X,Y,½(Z_x+Z_y),t)$.

Visualization of three-dimensional particle tracks is used to identify the convection patterns that are induced by evaporation from an open channel. In all the measurements performed, a single vortex has been observed. The formation of the vortex has been observed and measured. The vortex spreads from the meniscus region inward for at least 2.7mm. The dynamics of the vortex is studied by measuring the position and the speed of its frontline while it goes inwards (Section 4.4.2). The rotational speed of a completely developed vortex is quantified by measuring the speed of the particles going in the two directions (Section 4.4.3). We report vortex velocities taken using two solutions with low and high salt concentration. In Section 4.4.2 a control experiment in PBS where evaporation is prevented shows how the vortex flow field is dependent on evaporation.

4.4.2 Vortex frontline

In all the recordings the particles are observed to move in a similar way. The solution in the channel divides into two columns: one column flows upward towards the meniscus, while the other moves downward. Our interpretation is that a single vortex is formed from the meniscus surface towards the inner part of the channel.

To prove this, we recorded the motion of the particles inside the solution immediately after the channel is filled up. A single vortex is observed to develop from the meniscus region (outside of the region under observation) inward until occupying the whole observed region. This result can be observed in Fig. 56, where the image is obtained by applying a level filter and a

motion blur filter to a set of images from one of the two projections, so that the particle traces can be observed in a single picture.

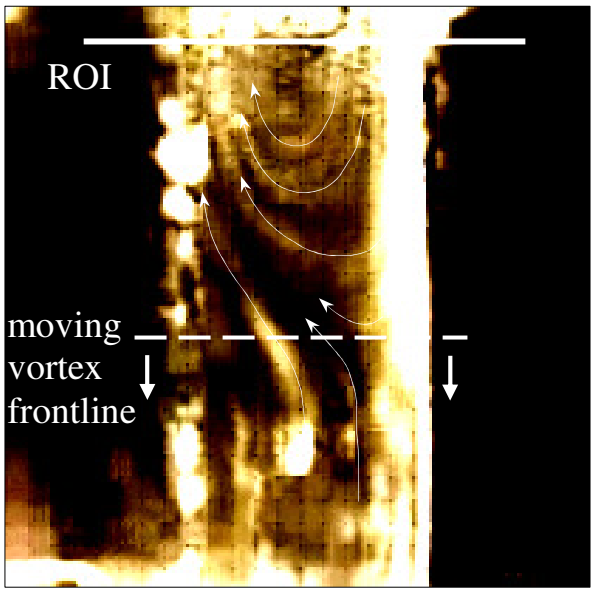

Fig. 56 Traces of the vortex genesis. The frontline of the vortex (dashed line) moves down with time. The continuous line defines the top of the region under observation.

The vortex front is defined as the lowest vertical position of the particle traces that close to itself in a circular manner (the tracks above the dashed line in Fig. 56). The vortex front is measured with time in solutions of different salinity. Typical vortex front velocities for PBS and KCl 0.8M are shown in Fig. 57 and Fig. 58.

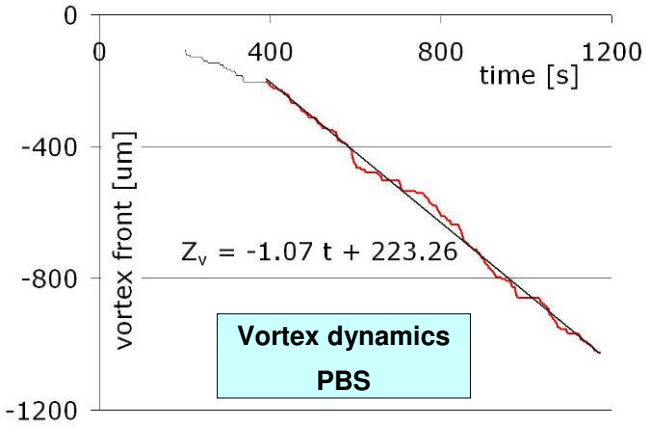

Fig. 57 Vortex generation in PBS

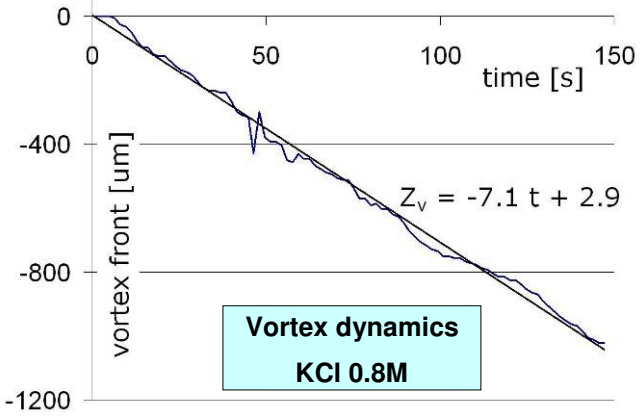

Fig. 58 Vortex generation in KCl0.8M

In the Y-axis the vertical position of the vortex frontline is plotted. The zero value corresponds to the top of the region under observation (continuous line in Fig. 56), which is about 1200um long. In the X-axis it is shown the time since when the frontline entered in the region under observation. Unexpectedly the frontline descends with a linear behaviour with time, with the exception of the initial part in the case of PBS solution. The lack of an asymptotic behaviour suggests that the vortex reaches much deeper regions, of the order of one centimetre or more.

Linear regression is performed on the curves. The formulas of the linear fits are shown on the graphs. The parameter of interest is the angular coefficient, as it characterizes the speed of the generation of the vortex in the channel. The velocity of the generation of the vortex (v_g) is hence:

$$v_{g\,PBS} = 1.07 \text{ um/s} \tag{4.2}$$

$$v_{g\,KCl} = 7.1 \text{ um/s} \tag{4.3}$$

The vortex frontline velocity increases from 1um/s to 7um/s, a significant factor dependent only on a change in salinity of the solution.

4.4.3 Vortex characteristic velocities

As observed above, once the channel is filled to the top, a vortex forms until dividing the channel into two regions, one flowing towards the outlet, the other towards the inlet. In the previous chapter we have also seen that solutions with different salinity are characterized by a different speed with which the vortex invades the channel.

In this chapter, we show a further characterization of the vortex generated in different conditions of salinity. The characteristic speed of the two opposite flowing regions is measured when the vortex already invaded the visible micro-channel. We call these velocities v_{up} and v_{down}.

The velocity of the particles depend on the position in the flow. A good choice to characterize the flows is to measure the maximum speed of the flows. Therefore only the particles in the central portion of each flow are considered. We measured only the speeds of the particles in the central third of the channel, between the channel walls, and the area that separates the two

flowing columns. This area is easily individuated because in that region the particles are observed to move horizontally.

These flows can be characterized by the average speed in the central part of each region. Particles speed is measured from a single experiment, through elaboration of the recorded movie with the custom software described in section 4.3.1. A superposition of the histograms of the results for v_{up} and v_{down} in PBS are shown in Fig. 59 and in KCl in Fig. 60.

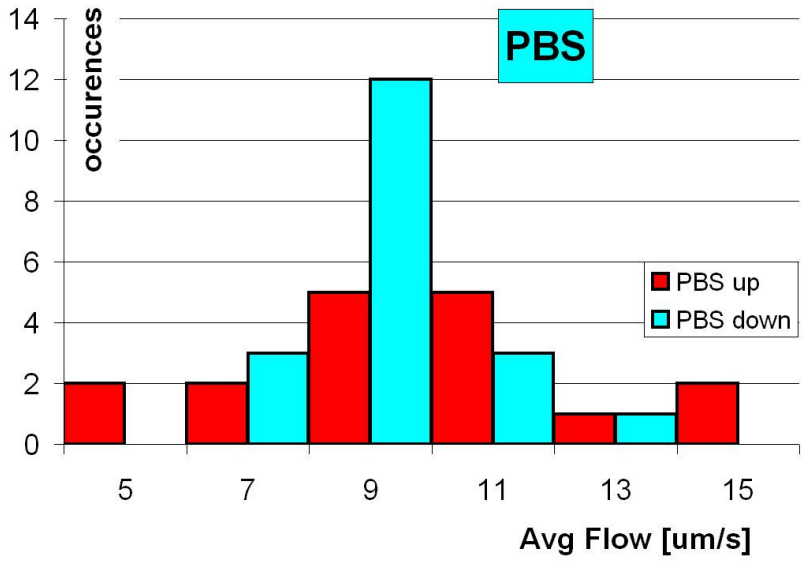

Fig. 59 Histogram of the velocity of particles in PBS. The red tiles represent the particles moving upward, and the light blue ones represent the particles moving downward.

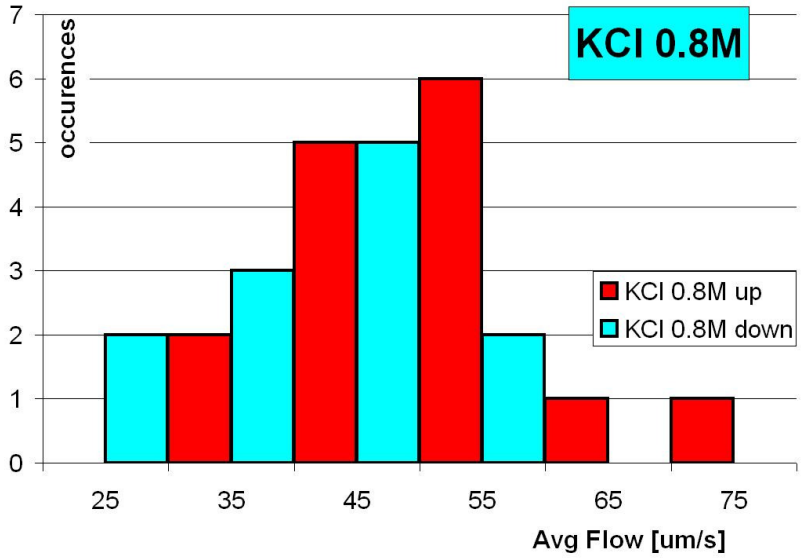

Fig. 60 Histogram of the velocity of particles in KCl 0.8M. The red tiles represent the particles moving upward, and the light blue ones represent the particles moving downward.

The measured particle velocities are the sum of the velocity of the flow with the gravitational fall of the particles. The calculations shown in section 4.3.3 suggest that the latter is negligible, thus the velocities here represented are a direct image of the flow field. PBS values average around 9.5um/s, with the upward stream slightly faster (9.8um/s) than the downward one (9.0um/s). This is counterintuitive because we should expect that the two streams equal. Evaporation though could play a role also in this phenomenon, because, as we have seen in Chapter 2, the evaporative flow rate per unit area is of the order of 1um/s, accountable for such a difference.

An even more pronounced difference can be observed for the KCl data, where v_{up} is 50.0um/s and v_{down} is 40.5um/s. A possible answer is that the two flows don't have the same cross section, so a different distribution in the velocity of the flow could even out a difference in cross sections.

4.4.4 Inhibited evaporation

The objective of the experiments described so far is to better understand what type of influence, if any, does the evaporation at the meniscus surface have on an inner region, more than 1mm deep inside a microchannel. The results show how a vortex develops and occupies a region longer than 2.7 millimetres. The experiments show a definite phenomenon, but a negative experiment needs to be addressed. Removing the supposed cause we in fact expect that also the phenomenon is not observed anymore. In that case we can be sure that the vortex generation and dynamics depends on surface effects due to evaporation.

To this aim we describe in this section an experiment performed in PBS where the only difference with the experiments described before is that evaporation is inhibited. A cap built in PDMS and glass is posed at the exit of the micro-channel. Glass is used to assure full optical access, while a well of 2mm in diameter and 1mm in height is obtained in the PDMS. The cap creates a closed region, where evaporation occurs only until the saturation vapor pressure is reached. The small dimensions of the well in the cap, chosen to minimize the volume and to allow for easy alignment, forces evaporation to be inhibited after a short time (<1m) from the beginning of the experiment.

As expected, the flow is observed to be very stable. No vortex is observed, and a homogeneous downwards motion of the trackers is measured and shown in Fig. 61.

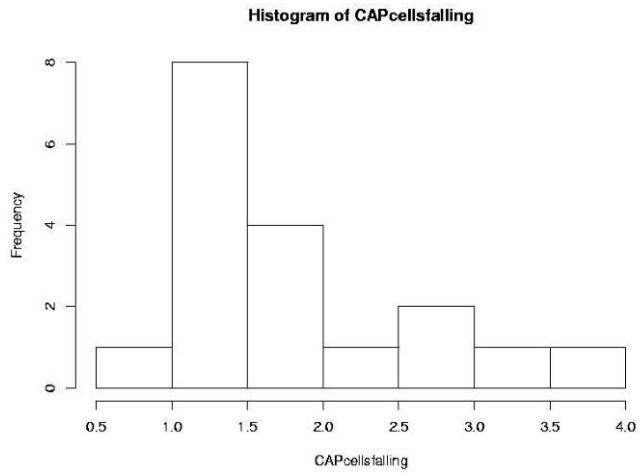

Fig. 61 Histogram of particle falling velocity in PBS. Evaporation is inhibited.

The average velocity is 1.8um/s, which is compatible with the expected gravitational fall of cells in PBS (section 2.1.1, eq.2.7).

4.5 Summary

This chapter presents an investigation of the flows inside open microfluidic channels induced by evaporation. The velocity field 1mm inside the microchannel below the meniscus, is traced using a novel method for three-dimensional flow visualization. With a custom built device it is possible to reconstruct the XYZ view of the channel and of the particles inside it.

Once the channel is filled to the top, a single vortex generates until dividing the solution in the channel into two parallel channels, one flowing towards the outlet, the other towards the inlet. Solutions with different salinity are characterized by a different speed with which the vortex invades the channel and by different vortex rotational speed.

In order to use the evaporation to aid particle position control against gravitational fall, it is important to understand all the effects of evaporation in the flow field. The ability to control these flow field could in principle be an alternative technique to move particles in open microfluidic networks, decreasing the stress on the particles that would just be gently pushed by induced convective flows as desired.

5 Conclusions

The work presented in this thesis reports theory and experiments aimed at taking advantage of evaporation phenomena to counteract the gravitational fall of living cells in open microfluidic systems. Evaporation generates an upward flow maintained by capillarity through a phenomenon known as transpiration. Evaporation depends on environmental parameters such as temperature and relative room humidity, as well as it depends on the evaporating surface, related to the meniscus shape.

A custom electrical device is designed and fabricated to measure the meniscus height. An original strategy is conceived to optically measure the evaporative flow rate. The two experimental strategies allow us to correlate the capacitance measurements with the evaporative flow rate for a meniscus sensor able to detect the evaporative flow rate. Particular attention lays on the electrical optimization of such device, which shall be integrated in an array of biosensors/bioactuators.

Another custom device, designed to allow three-dimensional optical access to a microchannel is used to map the 3D flow pattern originated at the meniscus by phenomena related to evaporation of saline solutions. In a region far from the meniscus the generation of a single vortex is observed and characterized.

6 Selected bibliography

[**1**] H. Lee, Y. Liu, D. Ham and R. W. Westervelt, "Integrated cell manipulation system-CMOS/microfluidic hybrid", *Lab on a Chip*, Vol 7, pp.331-337, 2007

[**2**] M. Castellarnau, N. Zine, J. Bausells, C. Madrid, A. Juarez, J. Samitier, and A. Errachid, "Integrated cell positioning and cell-based ISFET biosensors", *Sensors and Actuators B*, 120, 2007, pp.615-620

[**3**] A. Heeren, C. P. Luo, W. Henschel, M. Fleischer, and D. P. Kern, "Manipulation of micro- and nano- particles by electro-osmosis and dielectrophoresis", *Microelectronic Engineering*, 84, 2007, pp.1706-1709

[**4**] Alexandra B. Fuchs, Aldo Romani, Delphine Freida, Gianni Medoro, Melanie Abonnenc, Luigi Altomare, Isabelle Chartier, Dorra Guergour, Christian Villiers, Patrice N. Marche, Marco Tartagni, Roberto Guerrieri, Francois Chatelaina and Nicolo Manaresi, "Electronic sorting and recovery of single live cells from microlitre sized samples", *Lab on a Chip*, Vol. 6, pp.121-126, 2006

[**5**] U. Lehmann, M. Sergio, S. Pietrocola, C. Niclass, E. Charbon, and M. A. M. Gijs, "A CMOS microsystem combining magnetic actuation and in-situ optical detection of microparticles", *Transducers 2007*, Lyon, June 2007, pp.2493-2496

[**6**] H. Morgan and N. G. Green, "AC Electrokinetics: colloids and nanoparticles", Research Studies Press LTD, England, 2003

[**7**] H. K. Walker, W. D. Hall, and J. W. Hurst, "Clinical methods, the history, physical, and laboratory examinations", Ed. Butterworths

[**8**] L. E. Bottinger, and C. A. Svedberg, "Normal erythrocyte sedimentation rate and age", *British Medical Journal*, Vol 2, 1967, pp.85-87

[**9**] Otto Klement, Fantastic Voyage, 1966. The movie that inspired the novel written by Isaac Asimov

[**10**] Coulie et al. "T-cell responses of vaccinated cancer patients". Curr Opin Immunol. 2003; 15(2):131-7

[**11**] Van Der Bruggen et al., "Tumor-specific shared antigenic peptides recognized by human T cells". Immunol Rev. 2002;188:51-64

[**12**] Morgan et al. "High efficiency TCR gene transfer into primary human lymphocytes affords avid recognition of tumor antigen glycoprotein 100 and does not alter the recognition of autologous tumor antigens". J Immunol. 2003;171(6):3287-95

[**13**] Kawarada et al. "NK- and CD8(+) T cell-mediated eradication of established tumors by peritumoral injection of CpG-containing oligodeoxynucleotides". J Immunol. 2001; 167(9): 5247-53

[**14**] A. Romani, N. Manaresi, L. Marzocchi, G. Medoro, A. Leopardi, L. Altomare, M. Tartagni, R. Guerrieri, "Capacitive sensor array for localization of bioparticles in CMOS Lab-on-a-CHIP", *Proc. of ISSCC* 2004

[**15**] M. Abonnenc, L. Altomare, M. Baruffa, V. Ferrarini, R. Guerrieri, B. Iafelice, A. Leonardi, N. Manaresi, G. Medoro, A. Romani, M. Tartagni and P. Vulto, "Teaching cells to dance: the impact of transistor miniaturization on the manipulation of populations of living cells", *Solid State Electronics*, Vol. 49 (5), pp.674-683, 2005

[**16**] V. Namasivayam, R. G. Larson, D. T. Burke, and M.A. Burns, "Transpiration-based micropump for delivering continuous ultra-low flow rates", *J. of Micromechanics and Microelectronics,* vol. 13, pp.261-271, 2003

[**17**] G. Franco, "Progetto di un sistema di regolazione del flusso evaporativo per il controllo della posizione di particelle in dispositivi microfluidici", Bachelor thesis Bologna University, 2006

[**18**] M. Zimmermann, S. Bentley, H. Schmid, P.Hunziker, and E. Delamarche, "Continuous flow in open microfluidics using controlled evaporation", *Lab on a Chip*, Vol. 5, pp.1355-1359, 2005

[**19**] Y. Chou, Y. Chen, and S. Kang, "Study of evaporation phenomena in micro channels", *Proceedings of IEEE-NEMS 2006,* Zhuhai, China, January 2006

[**20**] X.Zhang, H. He, Y. Xu. T.H. Gong, F.Eng Hock Tay, "An improved approach for precise in situ measurements of microflows", *Review of Scientific Instruments*, vol. 73, n. 3, pp.1185-1187, March 2002

[**21**] S. Billat, K. Kliche, R. Gronmaier, P. Nommensen, J. Auber, F. Hedrich, and R. Zengerle, "Monolithic integration of micro-

channels on disposable flow sensors for medical applications", *Transducers 2007*, Lyon, June 2007, pp.29-32

[**22**] C. Chen, F. Tseng, and C. Chieng, "Evaporative evolution of volatile liquid droplets in nanoliter well array", *Transducers 2005*, Seoul, Korea, June 2005, pp.812-815

[**23**] Ashrae Handbook, Fundamentals, Chapter 8, Atlanta (1997).

[**24**] J. P. Holman, "Heat Transfer", SI Metric Edition, pp.593-595, *McGraw-Hill* Book Company, USA, 1989

[**25**] Z.Chen, A.A.Darhuber, S.M.Troian, S.Wagner, "Capacitive sensing of droplets for microfluidic devices based on thermocapillary actuation", *Lab on a Chip*, Vol. 4, pp.473-480, 2004

[**26**] G. Franco, "Progetto di un sistema di regolazione del flusso evaporativo per il controllo della posizione di particelle in dispositivi microfluidici", Bachelor thesis Bologna University, 2006

[**27**] S. Mauriello, "Caratterizzazione di biosensori in tecnologia PCB", Bachelor thesis Bologna University, 2006

[**28**] B. Timmer, W. Sparreboom, W. Olthuls, P. Bergveld, A. van der Berg, "Optimization of an electrolyte conductivity detector for measuring low ion concentrations", Lab on a Chip, Vol. 2, pp.121-124, 2002

[**29**] E.Jung, D. Manessis, A. Neumann, L. Böttcher, T. Braun, J. Bauer, H. Reichl, B. Iafelice, F. Destro, and R. Gambari, "Lamination and laser structuring for a DEP microwell array", Proc. DTIP 2007, Stresa, April 2007, pp.51-156

[**30**] B. Iafelice, F. Destro, D. Manessis, D. Gazzola, E. Jung, L. Boettcher, M. Borgatti, T. Braun, J. Bauer, R. Gavioli, R. Gambari, A. Ostmann, and R. Guerrieri, "Aluminium printed circuit board technology for biomedical micro-devices", Proc. of *MicroTAS 2007 Conference*, Paris, October 2007, pp.563-565

[**31**] S. Gawad, K. Cheung, U. Seger, A. Bertsch, and P. Renaud, "Dielectric spectroscopy in a micromachined flow cytometer: theoretical and practical considerations", *Lab on a Chip*, Vol. 4, pp.241-251, 2004

[**32**] E. Pierpaoli, "Ottimizzazione di un rivelatore impedenziometrico di menisco mediante diverse configurazioni di elettrodi", Bachelor thesis Bologna University, 2007

[**33**] C.A. Ward and F. Duan, "Turbulent transition of thermocapillary flow induced by water evaporation", *Phys Rev E*, Vol. 69 (5), 2004

[**34**] P. Chamarty, H. K. Dhavaleswarapu, S. V. Garimella, J. Y. Murthy, S. T. Wereley, "Visualization of convection patterns near an evaporating meniscus using uPIV", *Experiments in Fluids*, Vol. 44(3), pp.431-438, 2007

[**35**] C. Buffone, K. Sefiane, "IR measurements of interfacial temperature during phase change in a confined environment", *Experimental Thermal and Fluid Science*, Vol. 29, pp.65-74, 2004

[**36**] H.Wang, J. Y. Murthy, S. V. Garimella, "Transport from a Volatile Meniscus Inside an Open Microtube", International Journal of Heat and Mass Transfer, In Press 2007

[**37**] K. Wozniak, G. Wozniak, T. Roesgen, ”Particle-image-velocimetry applied to thermocapillary convection”, *Exp fluids*, Vol. 10(1), pp.12-16, 1990

[**38**] Y. Kamotani, S. Ostrach, A. Pline, “Analysis of velocity data taken in surface-tension driven convection experiment in microgravity”, *Phys Fluids*, Vol. 6(11), pp.3601-3609, 1994

[**39**] M.G. Braunsfurth and G.M. Homsy, “Combined thermocapillary-buoyancy convection in a cavity. Part II. An experimental study”, *Phys Fluids*, Vol. 9(5), pp.1277-1286, 1997